

(GRANT AGREEMENT: 661880)

DELIVERABLE 2.9 **Evolution of stress in biotic and abiotic clay flow cells**

Editors: Simon Gregory, UKRI BGS

Kay Green, UKRI BGS Jon Harrington, UKRI BGS Lorraine Field, UKRI BGS Simon Kemp, UKRI BGS Keith Bateman, NERC BGS

Date of issue of this report: 13.07.2018

This project has received funding from the Euratom research and training programme 2014-2018 under Grant Agreement no. 661880							
	Dissemination Level						
PU	PU Public						
PP	Restricted to other programme participants (including the Commission)	PP					
RE	Restricted to a group specified by the partners of the MIND project						
СО	Confidential, only for partners of the MIND project						

Publishable Summary

Microbial activity has been implicated in both the corrosion of steel material and alteration of bentonite clays used in geological disposal facilities for radioactive waste. To understand the limits on microbial growth and the potential for microbial activity in this environment to affect the swelling behaviour of the clay and metal corrosion, a series of laboratory experiments were performed. The experiments described here were designed to investigate multiple effects of microorganisms (on steel corrosion, changes to bentonite swelling capacity, permeability and fluid flow) in a single set of laboratory scale flow experiments using compacted bentonite samples. Bentonite samples were prepared by mixing y-irradiation-sterilized bentonite powder and artificial groundwater in a precalculated ratio, then compacting them using a hydraulic press to achieve a final dry density of 1400 kg m⁻³. Five grams of steel chips were incorporated into the sample in a thin layer near the inlet end of fluid flow. Sterile samples were compared to samples inoculated with an enrichment of sulphate reducing bacteria from the un-irradiated clay. Experiments were run in the presence and absence of sodium lactate to stimulate microbial growth. The results presented here relate to the development of stress in the experiments, including discussion of petrological and mineralogical alterations that could influence the physical properties of the bentonite.

There was evidence of steel corrosion in all experiments, detected by visual and microscopic observation and XRD analysis. XRD data showed an increase in the basal spacings of smectites in the zone immediately surrounding the steel compared to the starting material and material taken from further away from the steel, indicating replacement of monovalent cations with divalent ones. At large scales this could have the effect of reducing swelling capacity of the clay. There was also some indication that basal spacing was smaller in the presence of microorganisms, however more data from later experiments will be required to confirm this.

Close examination of the bentonite around the corroded steel by SEM in the uninoculated experiment without lactate (BUG021), showed strong Fe enrichment within the bentonite, with Fe coating (or replacing) the bentonite. Some calcium precipitation was observed by element mapping, but no identifiable crystal morphologies observed. Initial stub analysis of the lactate-amended uninoculated experiment (BUG023) did not reveal any obvious iron enrichment or calcium precipitation. In comparison, in both of the inoculated experiments, the material around the corroded steel was characterised by calcium enrichment and observation of acicular calcium carbonate crystals within fractures in the bentonite next to the steel. A fibrous iron-rich phase was observed in the bentonite, and in the case of the lactate-amended, inoculated experiment (BUG023), precipitating over the acicular calcium carbonate. In context of previous work in the literature, this was interpreted as being a result of cracks opening up around corroding steel as water within the bentonite is consumed by the corroding steel causing the clay to shrink back. This water movement may be responsible for the observed calcium enrichment and iron diffusion into these fractures. Further experiments are required to confirm that microorganisms from the sulphate reducing enrichment community involved in the aragonite precipitation in the inoculated experiments.

The continuous monitoring of the CVAF vessels allowed the evolution of swelling pressure and the permeability values for each sample to be monitored. There was a notable difference between the lactate amended experiments (BUG022 and BUG024) and unamended experiments (BUG021 and BUG022). In unamended experiments the values for swelling pressure at the end of testing were higher than those obtained prior to hydraulic testing, suggesting some form of reaction has occurred causing expansion of the fabric. It may be that this is related to the reduced amount of divalent substitution seen in the lactate amended samples by XRD analysis, possibly as a consequence of additional sodiums irons coming from the sodium lactate. Unfortunately, any effect that microbial activity had on the evolution of stress in the clay samples was too small for detection using our

system. Given the localised nature of corrosion within the clay, longer term testing of samples with iron dispersed within the sample are required to confirm and contextualise these results and its understand its potential impact on performance assessment.

Contents

1	Intr	oduc	tion	1
2	Me	thods	5	1
	2.1	Ехр	erimental system	1
	2.2	Cali	bration	3
	2.3	Sam	nple preparation	3
	2.3.	.1	Preparation of sample	3
	2.3.	.2	Preparation of inocula	5
	2.4	Phy	sical properties of prepared samples	5
	2.5	CVA	AF experimental methodology	5
	2.6	Pos	t experimental sample processing	6
	2.7	Mic	robiological analyses	7
	2.7.	.1	Most probable number counts	7
	2.7.	.2	Miles Misra plate counts	7
	2.8	X-ra	y diffraction (XRD) analysis	7
	2.9	SEN	1 analysis	8
	2.9.	.1	Scanning electron microscopy and X-ray microanalysis	9
3	Res	ults		10
	3.1	Initi	al swelling pressure of the clay	10
	3.2	SEN	1 analysis	13
	3.2.	.1	BUG021 (1400 kg m ⁻³ dry density, sterile, no lactate)	13
	3.2.	.2	BUG022 (1400 kg m ⁻³ dry density, inoculated, no lactate)	26
	3.2.	.3	BUG023 1400 kg m ⁻³ lactate amended, sterile	35
	3.2.	.4	BUG024 (1400 kg m ⁻³ dry density, lactate amended, inoculated)	37
	3.2.	.5		39
	3.3	XRD) analysis	39
	3.3.	.1	BUG021 uninoculated, no lactate added	39
	3.3.	.2	BUG022 inoculated, 1400 kg m ⁻³ no lactate added	40
	3.3.	.3	BUG023 inoculated, 1400 kg ^{m-3} lactate added	41
	3.4	Mic	robiological analysis	41
4	Disc	cussic	on	43
5	Ack	nowl	edgement	47
6	Ref	erenc	res	47

1 Introduction

The potential for microorganisms to survive the extreme environments generated around a GDF have been established in many studies [1] for reviews, [2], see [3], but further work is required to establish rates and limits of microbial activity, and more importantly, the impact that this activity could have on the GDF safety case. Understanding microbial activity in two key areas is particularly important: microbial activity within bentonite and microbially influenced corrosion (MIC). Microbial activity within bentonite clays is important as this could affect their swelling capacity, and therefore ability to act as a barrier to flow. Microbial activity can enhance corrosion rates, which could have impacts on the lifetime of the canisters and on production of hydrogen in a GDF.

There is a growing body of evidence that microorganisms are present in both natural clay host rocks [4]–[8] and in industrial bentonites that will be used as buffer materials in the design of a GDF [9], [10]. In clay formations or compacted bentonite, microbial biomass and activity is likely to be limited, due to a combination of factors including limited pore spaces, accessible carbon sources and water availability [11] and but studies show that viable microbes persist even under repository conditions [12]–[14], but it is generally considered that many of the microbe might be surviving in dormant states or as spores [14], [15].

In other environments, such as soils or depleted hydrocarbon reservoirs, the microbial action of bacterial has been shown to reduce the swelling capacity of clays [16], [17], and although it has been suggested to occur in the context of radioactive waste repositories [18], [19]. The extent to which this can occur in compacted bentonite within a GDF environment is not well understood. The cause of the loss of swelling capacity is thought to be iron reducing microorganisms bringing about the conversion of smectite to illite [18], [20]. The associated loss of swelling capacity has the potential to negatively impact on the effectiveness of the bentonite to act as a barrier to movement of groundwater and radionuclides.

In addition to altering clay properties, microorganisms have been implicated in corrosion of metals used, for example in canister material [21]–[24]. As many microorganisms e.g. sulphide and acetate producers, use H_2 as an electron donor, hydrogen scavenging by microorganisms may accelerate anaerobic corrosion of iron. Hydrogen generated by microbial or abiotic corrosion fuels the metabolism of these organisms. The resultant the metabolic products may be corrosive e.g. sulphide is corrosive for both iron and copper and acetate can cause stress cracking in copper. This increases the corrosion of metals and provides further hydrogen to support microbial activity.

Therefore, there is need to understand the limits to microbial growth and the potential for microbial activity to affect the swelling behaviour of the clay and metal corrosion. As described, survival in bentonites, alteration of swelling capacity and microbial steel corrosion have all been investigated in isolated. The experiments described here were designed to investigate all these processes in in a single set of laboratory scale flow experiments using compacted bentonite samples. The results presented here relate to the development of stress in the experiments, including discussion of petrological and mineralogical alterations that could influence the physical properties of the bentonite.

2 Methods

2.1 Experimental system

All experiments were run as flow experiments in pressure vessels, instrumented to monitor pressures and flows. The experimental apparatus is shown in Figure 1. The constant volume and axial flow (CVAF) apparatus was designed to examine the sensitivity of swelling pressure and permeability to

the corrosion of iron compacted within the bentonite clay. There are six main components to the experimental system: (1) a thick-walled stainless steel pressure vessel, (2) a fluid injection system, (3) a backpressure system, (4) five total stress sensors to measure radial and axial stress [5] a port at the mid-plane of the sample to measure porewater pressure, and (6) a microcomputer-based data acquisition system, Figure 1. To maximise the number of tests that could be run in the time available, the test system was replicated so that two independent systems could be used simultaneously to double the rate of data collection.

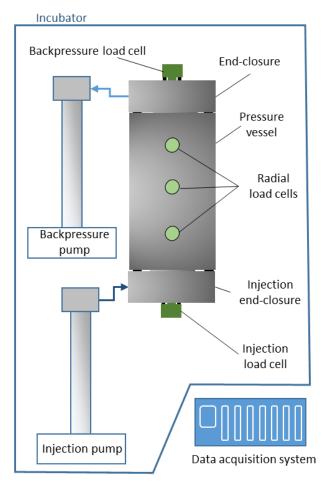


Figure 1 Schematic showing the main components of the constant volume and axial flow (CVAF) apparatus. The pressure vessel was mounted vertically to avoid gravity effects during flow testing

Each pressure vessel comprised a dual-closure tubular vessel manufactured from titanium and pressure-tested at 69 MPa. Each of the end-closures were secured by eight high tensile cap-screws which could also be used to apply a small pre-stress to the specimen if required. Figure 2 is a cut-away section showing the two end-closures with their embedded drainage filters and the axial total stress sensors. The 50 mm internal bore of the pressure vessel was honed to give a highly-polished surface. The stress gauges were an in-house design which use a 10 mm titanium push-rod fitted with an "O"-ring seal which acts directly upon a load cell located within a housing (bolted to the external surface of the pressure vessel). Each load cell was manufactured by Burster and rated between 2 and 5 kN.

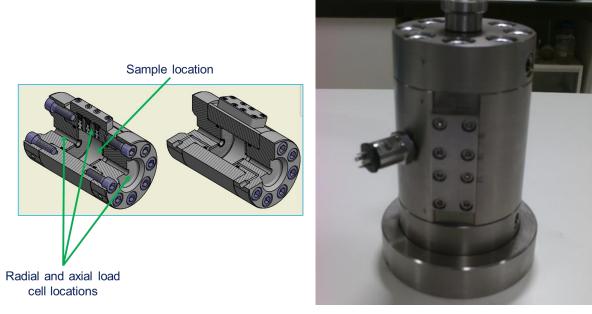


Figure 2 Schematic showing the cut-away section of the CVAF pressure vessel (left) and a photograph of the vessel before plumbing in to the flow system (right).

Volumetric flow rates for each apparatus were controlled or monitored using a pair of Teledyne-ISCO syringe pumps operated from a single digital control unit. One experimental system was equipped with a set of DM100 pumps and the other D260 pumps. The position of each pump piston was determined by an optically encoded disc graduated in segments equivalent to a change in volume of 4.8 and 16.6 nL respectively. Movement of the pump piston was controlled by a microprocessor, which continuously monitored and adjusted the rate of rotation of the encoded disc using a DC-motor connected to the piston assembly via a geared worm drive. This allowed each pump to operate in either constant pressure or constant flow modes. A programme written in LabVIEWTM elicited data from the pump at pre-set time intervals. Testing was performed within an incubator at 35°C located in an air-conditioned laboratory at a nominal temperature of 20°C.

2.2 Calibration

All stress and pressure sensors were calibrated against laboratory standards by applying incremental steps in pressure, from atmospheric to a pre-determined maximum value. This was followed by a descending history to quantify hysteresis. Least-squares fits were calculated, and the regression parameters used to correct raw data.

2.3 Sample preparation

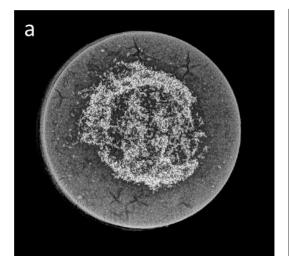
2.3.1 Preparation of sample

To investigate the interactions between microorganisms, bentonite clay and steel, composite compressed clay samples were prepared. Irradiated powdered FE Bentonite (obtained from NAGRA) was combined with 5 g "unalloyed steel chips" (DH-SE21-14 LGC Standards) and artificial groundwater based on Grimsel groundwater (5.6 mg/l Ca, 0.15 mg/l K, 5.3 mg/l Cl, 5.5 mg/l SO₄, 15.5 mg/l Na). To sterilise samples, the bentonite was irradiated at Manchester University's Dalton Facility, Cumbria (dose rate range of 30 Gy to 53.1 Gy), steel and groundwater were sterilized by autoclaving at 121°C for 15 min. All other containers and utensils used in the sample preparation were autoclaved or washed with 70% methanol prior to use if they could not be autoclaved. In between experiments, the CVAF and tubing was washed with 70% methanol under a pressure of 1.00 MPa.

Compacted bentonite samples containing steel chips were prepared to a dry density of 1400 kg m⁻³. The sterile bentonite powder was mixed in a food blender for 30 seconds to break down any lumps. The bentonite powder was then mixed with groundwater in a large beaker under anoxic conditions by hand for 30 minutes. The volume of groundwater used was calculated from the dry density required. To prepare the sample, approximately \% of the bentonite mixture was poured into the former (Figure 3) and tamped down using a spoon spatula. Next, 5 g steel was poured onto the centre of this layer using a powder funnel to ensure the layer remained central and the remainder of the bentonite mixture was added and tamped down. To compress the sample the plunger was placed into the former and the sample was compressed to a pressure of 11.13 MPa for 20 hours in a hydraulic press (Figure 3). After this time, the former was removed from the press and the sample was extruded from the press and immediately placed in a sterile plastic bag. Samples were measured and weighed in a Class II laminar flow hood to maintain sterility, and the bulk density was calculated (Table 1). Figure 4 shows x-ray images of a prepared sample that was not used for any of the experiments. The lighter area in the centre of image 4a, and towards the bottom of image 4b shows the position of the steel fragments (lighter colour on the image). Although exposure to the atmosphere could not be avoided completely while assembling the apparatus, these times were kept to a minimum.



Figure 3 Steel former and plunger (left) were inserted into the hydraulic press (right) to prepare the sample to a known dry density.



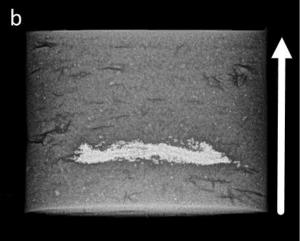


Figure 4 X-ray of prepared sample (note this sample was an early test sample, not used in any experiment. Longer compression times were used for experimental samples which resulted in a more homogenous clay appearance). (b)shows orientation of sample and direction of flow when in the CVAF

2.3.2 Preparation of inocula

For the inoculated experiments, a sulphate reducing bacterial (SRB) enrichment was prepared by inoculating approximately 150 ml Postgates medium B (0.5 g Γ^1 KH₂PO₄, 1.0 g Γ^1 NH₄Cl, 1.0 g Γ^1 CaSO₄2.0 g Γ^1 MgSO₄.7H₂O, 3.5 ml Γ^1 sodium lactate, 1.0 g Γ^1 yeast extract, 0.1 g Γ^1 , ascorbic acid, 0.1 ml Γ^1 thioglycolic acid, 0.5 g Γ^1 FeSO₄.7H₂O). Postgate's Medium B was prepared using tap water, adjusted to pH 7-7.5 before autoclaving. For the enrichment culture, 1g un-irradiated FE bentonite was used as the inoculum. Enrichment cultures were prepared in glass bottles in an anaerobic environment (95% N₂, 5% H₂), crimp sealed with a butyl rubber cap and grown at 35°C. The development of black precipitate in enrichment cultures indicated microbial sulphide production. When this happened, the supernatant was decanted and placed in a new bottle, the residual clay was reinoculated with fresh Postgates medium B. After growth of the enrichment cultures, the supernatant containing SRB was carefully poured into a centrifuge tube and the cells collected by centrifugation at 3350 x g for 5 minutes, and the pellet was washed twice with the artificial groundwater to remove traces of the Postgate's medium. The groundwater containing the SRB enrichment was used to prepare the sample, ensuring that the SRB were well distributed throughout the sample at the start of the experiment. The number of SRB present was calculated using MPN

2.4 Physical properties of prepared samples

Table 1, shows the basic physical properties of each test specimen. As preserved sample material was required for post-mortem analysis it was not possible to oven dry the sample (in order to determine the basic geotechnical properties). Instead, bulk density was estimated by simply subtracting the mass of steel from the wet-weight of the sample which was then divided by the volume.

Table 1	Basic physical	properties of	the test specimens.
---------	----------------	---------------	---------------------

Specimen number	Inoculated	Lactate	Mass metal (g)	Length (m)	Diameter (m)	Estimated bulk density (Mg.m ⁻³)
BUG021	No	No	4.73	47.50	49.96	1.83
BUG022	Yes	No	4.98	47.79	49.95	1.84
BUG023	No	Yes	5.00	51.72	49.82	1.86
BUG024	Yes	Yes	5.00	50.95	50.07	1.85

2.5 CVAF experimental methodology

Immediately following preparation and measurement, the sample was sealed into the CVAF vessel which had previously been sterilised using 70% methanol. Following installation of the samples (test stage [0]), a pressure of 1.00 MPa was applied to both ends of each specimen to induce swelling of the clay. Following a swelling period of at least 30 days the injection pressure was increased to 2.50 MPa for the remainder of the experiment. The injection and back pressure, and the pressures at the load cells were automatically logged and were monitored throughout.

Table 2 Summary of experimental histories showing sample, stage numbers and type of stage (EQ = equilibration, $CPT = constant \ pressure \ test)$

Specimen number	Туре	Injection pressure (MPa)	Backpressure (MPa)	Length of time (days)
BUG021 [1]	EQ	1.00	1.02	23
BUG021 [2]	CPT	2.51	1.02	125
BUG022 [1]	EQ	1.01	0.99	24
BUG022 [2]	CPT	2.52	0.99	121
BUG023 [1]	EQ	1.00	1.00	29
BUG023 [2]	CPT	2.48	1.00	122
BUG024 [1]	EQ	1.03	1.00	31
BUG024 [2]	CPT	2.52	1.01	109

2.6 Post experimental sample processing

At the end of each experiment the pressures in both pumps were reduced to atmospheric pressure and the constant volume vessel was removed from the apparatus. Groundwater samples were taken for chemical and microbiological analysis from the injection and back pressure pumps. (Chemical analysis is not presented in this report.) Where possible a sample of water was collected from the tubing between downstream end of the CVAF vessel and the back pressure pump while the tube was still under pressure. This was typically less than 1 ml, so only very limited chemical analysis was carried out.

The sample was extruded from the CVAF vessel using a hydraulic press, and immediately placed in a sterile bag, photographed and cut into sections (as shown in Figure 5) using an isopropanol washed circular saw blade. Photographs were then taken of the cut sections. Each section was used for different analyses: thin sectioning/polished block and SEM stub analysis (A), microbiology (B), XRD (C) and a stored reference section (D). Microbiological analysis commenced immediately, all other samples were vacuum sealed and stored at 4°C until analysis. During the removal of the sample from the CVAF, handling and exposure to the atmosphere was kept to a minimum and sterile foil or bags were used to minimise the potential for contamination. However, some exposure to the atmosphere e.g. for a brief period during the extrusion of the sample from the vessel or cutting the sample was unavoidable.

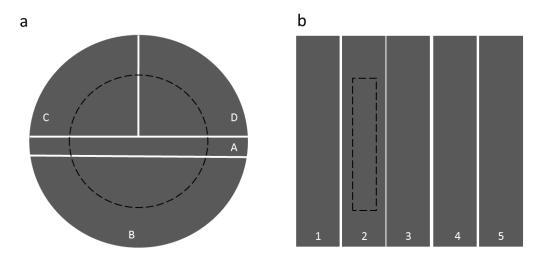


Figure 5 a) Illustration of the longitudinal cuts that were made in the post-experimental sample to allow the division for different analyses (thin sectioning/polished block for SEM and SEM stub analysis(A), microbiological analysis (B), XRD (C) and

reference section (D). b) transverse cuts made to the microbiology subsamples (B) (1= inlet end, 5 = outlet end). Dashed line shows approximate extent of steel containing layer.

2.7 Microbiological analyses

The section taken for microbiological analysis was cut into five equal subsamples (Figure 5b) in an anaerobic cabinet using a sterile scalpel. Subsample 2 always contained the steel chips. Using a fresh sterile scalpel, the outer surface of the clay was cut away to minimise any contamination that could have occurred during sample handling. The remaining bentonite was then cut into ~0.5-1 mm pieces and mixed using the scalpel. 1 g sample was taken for analysis. This was mixed with 5 or 6 ml 0.9% sterile saline and homogenised using a vortex. This slurry was used for culture based microbial enumeration. The remaining material was frozen at -20°C for future DNA analysis by quantitative PCR (qPCR) and microbial community analysis (results not presented here).

2.7.1 Most probable number counts.

Enumeration of key microbial groups is planned to be carried out using qPCR. For this, samples have been frozen and analysis will be carried out in a batch. In order to have some idea of changes to microbiology prior to qPCR, the following culture based methods were applied. Deep 96-well plates were used for MPN counts of sulphate reducing bacteria (using Postgate's medium B), and total aerobic and anaerobic heterotrophs (PTYG medium: peptone 5 gl⁻¹, tryptone 5 gl⁻¹, yeast 5 gl⁻¹, glucose 5 gl⁻¹, MgSO_{4.}7H₂O 0.6 gl⁻¹, CaCl_{2.}2H₂O 0.08 gl⁻¹). A dilution series was prepared from the slurry and 100 μ l of each dilution was used to inoculate three wells. Dilution series were also prepared from the samples taken from the injection and backpressure pumps. The final well of all 96 well plates was not inoculated and was used to identify contamination. All plates were incubated at 35 °C. Plates for anaerobic heterotrophs and SRB were sealed in Anaerocult® A mini A gas tight bags (Merck, Darmstadt, Germany) to maintain an anaerobic atmosphere. Positive wells were scored four weeks by the formation of a black precipitate in the Postgate's Medium and a cloudy appearance in the PTYG medium.

2.7.2 Miles Misra plate counts

Initial analysis on the first experiment showed that it was difficult to distinguish between the development of growth leading to cloudy medium and cloudiness caused by the presence of clay when using the PTYG media for heterotroph counts. Therefore, for subsequent tests a modified Miles Misra method [25] was used to count colony forming units of aerobic and anaerobic heterotrophs on PTYG agar plates. For this method eight 20 μ l aliquots of each dilution (2.7.1) were spotted onto the surface of an agar plate and number of colony forming units per ml was calculated from the mean of the eight drops.

2.8 X-ray diffraction (XRD) analysis

Preserved, sealed, damp core segment samples (section D in Figure 5) were submitted for X-ray diffraction (XRD) analysis. From these, four sub-samples were analysed. These were taken from: (1) the immediate inlet, (2) surrounding the corroded steel, (3) $^{\sim}1$ cm from the visible corrosion zone, (4) the extreme outlet edge of the sample. The subsamples were removed using a scalpel and dried overnight at 55°C. Subsamples were then crushed, and steel swarf removed using a hand magnet. A portion of the crushed material was then ground to a fine powder in an agate pestle and mortar and immediately front loaded into a cavity mount for random powder XRD analysis. Any remaining steel swarf was removed by stage-sieving on a 63 μ m cloth. Such analyses were carried out to determine the nature of any non-clay minerals present in the samples and also to determine the d060 spacing of any clay minerals present.

Subsequently, the clay mineral assemblages of the samples were studied by preparing oriented mounts. Typically, such analyses would be initiated by the isolation of a fine, $<2 \mu m$ size fraction to

increase the concentration of clay minerals. However, in this case, clay minerals form >75% of the MX-80 bentonite starting material [26] and therefore any such concentration is unnecessary. In addition, size separation of sodium bentonites is typically difficult as they form colloidal gels in water. Any requirement for the addition of a dispersing agent (typically sodium hexametaphosphate, 'Calgon') would also alter the exchangeable cation chemistry of the bentonite and its XRD characteristics. Therefore, in this study, material for oriented XRD mounts was prepared by further dispersing small (typically c.10 mg) portions of material in deionised water using ultrasound treatment and no dispersant was added. The dispersions were then pipetted onto glass slip substrates and allowed to dry at room temperature.

XRD analysis was carried out using a PANalytical X'Pert Pro series diffractometer equipped with a cobalt-target tube, X'Celerator detector and operated at 45 kV and 40 mA. The random powder mounts were scanned from 4.5 to 85°2 θ at 2.06°2 θ min⁻¹. Diffraction data were initially analysed using PANalytical X'Pert HighScore Plus version 4.6 software coupled to the latest version of the International Centre for Diffraction Data (ICDD) database.

The basal XRD spacings of smectite-group minerals are particularly susceptible to the prevailing humidity and temperature conditions when analysed. Therefore, in order to ensure constant conditions, both the random powder samples and air-dried oriented glass slip mounts were placed in an Anton Paar THC chamber attached to the diffractometer system and operated at 50% relative humidity and 40° C (Figure 6). Samples were conditioned at these settings for 30 min before scanning from $2-35^{\circ}20$ at $0.55^{\circ}20/\text{min}^{-1}$. The mounts were rescanned after glycol-solvation and after heating to 550° C for 2h with the chamber set to 40° C and ambient humidity.



Figure 6 Configuration of PANalytical X'Pert Pro diffraction system for analysis of oriented mount samples using an Anton Paar THC (controlled temperature and humidity) chamber; (a) analytical configuration, (b) close-up of the interior of chamber showing sample position with humid air supply tubing and chamber cover removed.

2.9 **SEM analysis**

The sub-sampled slice 'A' (Figure 1) was further subsampled by removing a thin slice from one edge, ensuring some corroded steel filings were captured. The thin slice was immediately placed in the scanning electron microscope for morphological and microanalysis. The remainder of slice 'A' was dried and vacuum-impregnated with epoxy-resin to stabilise the material before being thin sectioned or finished as polished blocks. A blue dye was added to the epoxy-resin to aid and facilitate the recognition of natural porosity. For the thin sections, the resin-impregnated blocks were mounted onto glass slides with colourless epoxy resin and ground to produce polished (48 x 28 mm) thin sections to a thickness of 100 μ m. This is thicker than for a standard thin section, and was necessary

because of the density contrast between the bentonite and the steel filings. The sections and blocks were finished by lapping with a 10 μ m aluminium oxide paste, and finally polishing with a 0.45 μ m diamond paste.

Low magnification images of the thin sections were recorded by digitally scanning the thin section using an Epson Perfection 1240U flatbed scanner equipped with a transmitted light (transparency) scanning attachment at a resolution of 1200 dpi.

2.9.1 Scanning electron microscopy and X-ray microanalysis

The sub-samples of the bentonite interface surface that had been in contact with the steel filings were examined in the uncoated state by scanning electron microscopy (SEM) in low-vacuum mode, using both secondary electron (SE) imaging and backscattered scanning electron (BSEM) imaging. The thin sections and polished blocks were examined in detail under BSEM operating conditions only. Element distributions in the bentonite matrix surrounding the steel filings were studied using digital energy-dispersive X-ray microanalysis (EDXA) elemental mapping and quantitative energy-dispersive electron probe point microanalysis (ED-EPMA). This was carried out simultaneously during backscattered scanning electron microscopy (BSEM). Both the thin sections and polished blocks were coated with a thin film (25 nm) of carbon by carbon evaporation under vacuum using an Agar turbo carbon coater, in order to make their surface electrically conductive for high-resolution SEM examination under conventional high vacuum mode (<1 x 10⁻⁴ torr).

BSEM imaging, EDXA and SE analyses were carried out using a FEI Company QUANTA600 environmental scanning electron microscope (ESEM) fitted with a 2-element (diode-type) backscattered electron detector, and equipped with an Oxford Instruments INCA 450 energy dispersive X-ray microanalysis (EDXA) system with a 50 mm² Peltier-cooled (liquid nitrogen free) silicon drift X-ray detector capable of operating at very high input X-ray count rates (up to $^{\sim}10^6$ counts per second). The scanning electron microscope instrument was operated in both low vacuum mode (0.95 torr) and conventional high vacuum mode (<1 x $^{\sim}10^{-4}$ torr), using a 10-20 kV electron beam accelerating potential, beam currents between 0.2 and 1.2 nA, and a working distance of 10 mm, as required. Phase identification was aided by microchemical information obtained from observation of EDXA spectra recorded from features of interest.

Digital EDXA X-ray element maps were recorded at a resolution of 1024 x 1024 pixels, and using a 20 kV electron beam, ~0.31 nA beam currents and a working distance of 10 mm, to give optimum X-ray count rates of up to 28,000 counts per second. EDXA spectra and digital X-ray elemental maps were processed using the INCA Microanalysis Suite version 5.05 (Oxford Instruments Analytical Limited, 2014) software package. X-ray element maps were produced by summation of data recorded from multiple frame scans to produce maps with sufficient X-ray counts per pixel to enable the key elements, required for the differentiation of the mineral species present, to be detected above background noise (typically between 20-50 frame scans, recorded over 0.5-2 hours). A reference BSE image was recorded for each mapped area. The image brightness in BSE images is related to the average atomic number of the phases observed [27], thereby enabling the differentiation of the different minerals present.

X-ray elemental maps were processed to show relative element concentrations using a 'rainbow colour scale' ranging from black (representing zero background) through green, yellow and orange (low to intermediate concentration) to red or white (representing high concentration). EDXA mapping observations focussed on the following elements:

- Carbon and chlorine maps indicate where epoxy-resin impregnates the samples.
- Silica, aluminium, and magnesium maps derived from the predominant silicate mineral assemblage in the bentonite.

- Sodium, potassium, and calcium are likely to be found as the exchangeable cation component of the
 smectite clay mineral that dominates the bentonite. Potassium and sodium are also recorded from Kfeldspar, albite and zeolites, and calcium from calcite that are also be present as minor components
 in the bentonite. Secondary precipitation of calcium reaction products is also feasible and sodium
 may also be recorded where sodium chloride derived from the experimental pore fluid may have
 been deposited.
- Iron maps primarily record the location of iron-rich alteration products. Accessory iron-bearing
 minerals within the bentonite such as pyrite and natural iron oxides (ilmenite, magnetite) would also
 be shown in the iron maps.
- Sulphur maps show where sulphur has been redistributed within the bentonite, and where secondary phases resulting from interaction with iron (e.g. iron sulphides or iron sulphates) might be present.

Semi-quantitative ED-EPMA compositional profiles were determined with longer X-ray count times than the mapping, and by rastering the electron beam over representative areas of bentonite. Profiles in each sample were taken perpendicular from the interface surface, into the bulk of the bentonite. Analytical data for key elements of interest e.g. iron, sulphur and calcium were recorded. Element concentrations were internally normalised relative to aluminium to allow chemical variations in the bentonite matrix to be easily compared. This is because of the heterogeneity in the bentonite at the scale of each analytical area that the ED-EPMA data were acquired from (due both to proportion of clay present, and to variations in the amount of resin impregnating the bentonite related to artefacts of shrinkage during sample drying and preparation). Aluminium was chosen as the normalising element, as it is present as a major element in the smectite (well above detection limits), and is relatively immobile compared to other more labile elements within the bentonite. An average background value was determined by averaging the data gained from rastering the electron beam over three separate fields of view taken of bulk bentonite within the distal thin sections.

3 Results

3.1 Initial swelling pressure of the clay

Following installation of the samples (test stage [0]), a backpressure was applied to both ends of each specimen to induce swelling of the clay, Table 2 test stage [1]. Figure 7 shows the response of tests BUG021 through BUG024 during this phase of the experiment. While there is some noise in the data, a transient response is clearly observed in all the tests which then evolves to a series of well-defined asymptotes. Close inspection of the data in BUG023 and BUG024, suggest the transient response may have been incomplete by the end of the stage as the stress traces exhibit a small positive gradient. However, estimates of swelling pressure during this phase of testing can be made and are presented in Table 3. Inspection of the data suggests that the swelling pressure for BUG021 is significantly lower than that developed in tests BUG022 through BUG024. However, there is some evidence in the data to suggest that samples BUG022 and BUG024 may have been subject to a small 'pre-stress' during the installation phase of each experiment. This has been observed to occur if the cap screws, which retain each end closure, are over-tightened to a higher torque leading to 'stressing' of the sample before hydration and swelling. However, there was little evidence for significant pre-stressing in sample BUG023 which exhibits a swelling pressure similar to that of BUG022. Comparing the data from Table 3 with estimates for bulk density presented in Table 1, shows no obvious linkage between these parameters, or, an explanation for the variance in the initial swelling pressure.

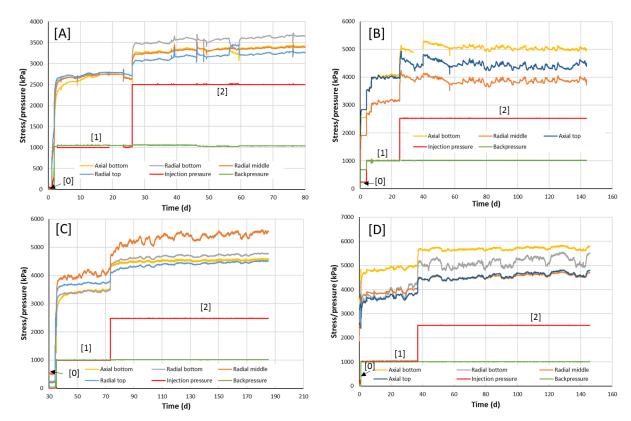


Figure 7 Development of axial and radial stress in tests BUG021 through BUG024 (letters A to D respectively) subject to the boundary conditions presented in Table 2. Numerical values in parentheses denote test stage numbers. Absolute values of stress should be treated with caution due to possible pre-stressing of the samples during installation.

Table 3 Initial swelling pressure for samples BUG021 through BUG024.

Specimen number	Test stage	Average swelling pressure (MPa)
BUG021	[1]	1.63
BUG022	[1]	2.74
BUG023	[1]	2.76
BUG024	[1]	3.37

Hydraulic properties of the clay

Following the hydration and initial swelling of the samples, a modest hydraulic gradient was applied across each specimen by raising the water pressure in the base (injection) filter to a pre-set value (Table 2). Inflow and outflow data were then measured as a function of time, Figure 8. In test BUG021, Figure 8[A], only a limited amount of outflow data was available due to problems with the control pump. However, when data became available the values closely matched those of the inflow data, suggesting minimal hydraulic storage and a fully saturated sample. This behaviour was also noted in tests BUG022 and BUG024, Figure 8 [B] and [D]. However, in test BUG023, Figure 8[C], outflow evolved more slowly, suggesting a significant period of time was required to reach steady state and thus attain hydraulic equilibrium. The reason for this difference remains unclear.

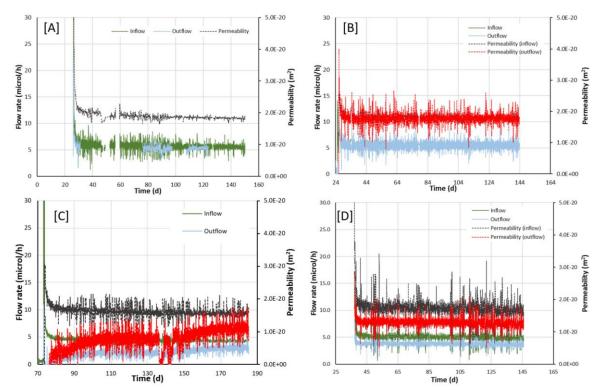


Figure 8 Time averaged hydraulic data from stage [2] of the experiments, showing inflow, outflow and permeability based on the flow data. Letters [A] through [D] denote experiments BUG021 through BUG024 respectively. Flow properties are presented in Table 4

Good mass balance (i.e. minimising the difference between inflow and outflow) was achieved in tests BUG021 and BUG022. The time-dependent outflow noted above in test BUG023 results in a miss-match between in- and outflow at the end of test stage [2]. Similarly, in test BUG024 a small offset between in and outflow was recorded, indicative of a small leak in either the injection or backpressure systems.

However, careful examination of the data suggests a slight reduction inflow/outflow in samples BUG023 and BUG024 compared to values for BUG021 and BUG022. This is reflected in the average permeability values, which also show a general reduction in the average permeability in samples BUG023 and BUG024.

The application of the hydraulic gradient also resulted in an increase in total stress observed throughout each specimen, Figure 7 test stage [2]. In all tests, stress rapidly increased following the application of the pressure gradient. This was followed by a period of less rapid stress evolution which slowly evolved into an equilibrium condition. However, in Figure 7[C], the stress values do not asymptote but continue to slowly increase. This was reflected in the hydraulic data, Figure 8[C], where the development of outflow lagged significantly behind inflow.

However, because the rate of change is very small, it is possible to estimate the swelling pressure of each sample at the end of hydraulic testing to examine what, if any, impact the fluid injection and microbial behaviour had on the mechanical behaviour of the clay, Table 5. While inspection of the data shows no clear trend, subtle changes in swelling behaviour may be present but obscured by limitations of the measurement system. That, combined with the small, localised zone of alteration within the clays, Section 3.2, means that changes in hydromechanical behaviour would be hard to detect on the time and scale of these experiments.

Specimen number	Test stage	Inflow (μl h ⁻¹)	Outflow (μl h ⁻¹)	Permeability - inflow (k) m ²	Permeability - outflow (k) m ²	Ave. permeability (k) m ²
BUG021	[2]	5.5	5.2	1.83E-20	-	1.83E-20
BUG022	[2]	5.6	5.5	1.80E-20	1.77E-20	1.78E-20
BUG023	[2]	4.1	3.2	1.49E-20	1.17E-20	1.33E-20
BUG024	[2]	4.8	3.7	1.65E-20	1.26E-20	1.46E-20

Table 5 Swelling pressure data for samples BUG021 through BUG024 before (stage [1], Table 3) and after (end of stage [2]) flow testing.

Specimen number	Test stage	Initial swelling pressure (MPa)	Final welling pressure (MPa)	Difference in swelling pressure (MPa)
BUG021	[2]	1.63	1.66	-0.03
BUG022	[2]	2.74	2.65	-0.09
BUG023	[2]	2.76	3.10	0.38
BUG024	[2]	3.37	3.45	0.08

3.2 **SEM analysis**

3.2.1 BUG021 (1400 kg m⁻³ dry density, sterile, no lactate)

A sub-sample was not taken from BUG021 due to the limited distribution of the steel filings. There was noticeable brown / yellow staining surrounding the iron filings. This is dark brown immediately surrounding the steel filings themselves (<1 mm penetration into the bentonite beyond the steel filings), and this fades to a yellowish staining which penetrates the bentonite a further 5 mm beyond the steel filings (Figure 9 & Figure 12).

The staining has penetrated in a radial nature around the steel filings rather than a unidirectional aspect i.e. starting from the steel filings and penetrating in the direction of flow (Figure 9). This indicates movement of iron was dominated by diffusion rather than advection. Under the SEM, the Fe-enrichment appeared very limited, extending just a few 10s of microns from the steel filings. Very little Fe is required to produce a stain visible optically in hand sample, so this will be caused by the fine dissemination of nanoparticles below optical and SEM resolution.

Optical microscopy indicated fine pyrite and dolomite throughout the bentonite. Cracks were also widespread (e.g. Figure 10 & Figure 11) – most of these were related to the drying of the sample for the thin sectioning process. However, some were formed during experimentation as they are lined with Fe-enrichment. Some fracturing occurred during the experiment as indicated by Figure 17A, although these may well have been enhanced (widened) as a result of post-experiment processing. The steel filings were shavings, so were embayed and stressed which has increased the surface area/weaknesses and therefore corrosion potential. The post-experiment fragments were more extensively embayed, and also many particles have an Fe-rich halo around them formed of coliform Fe which is a typical corrosion texture indicating some of these fragments have been partially to completely corroded.

SEM analysis showed strong Fe-enrichment within the bentonite, with a number of different textures. Fe-enhancement was very strong around the rims of some bentonite 'pellets' with the central cores showing little Fe-enhancement (Figure 16). This is indicative of bentonite pellets which will be more hydrated at the rims than the centre. Steel corrosion consumes water, dehydrating the bentonite. The wispy nature of the Fe-enrichment is due to precipitation within shrinkage cracks opening up as the bentonite dehydrates. The sharp boundaries noted were the hydration front. The cores of the bentonite were less dehydrated, so these still relatively unaltered (Figure 17). This also suggests the pellet boundaries have acted as pathways for Fe migration. Fe-migration is also illustrated by

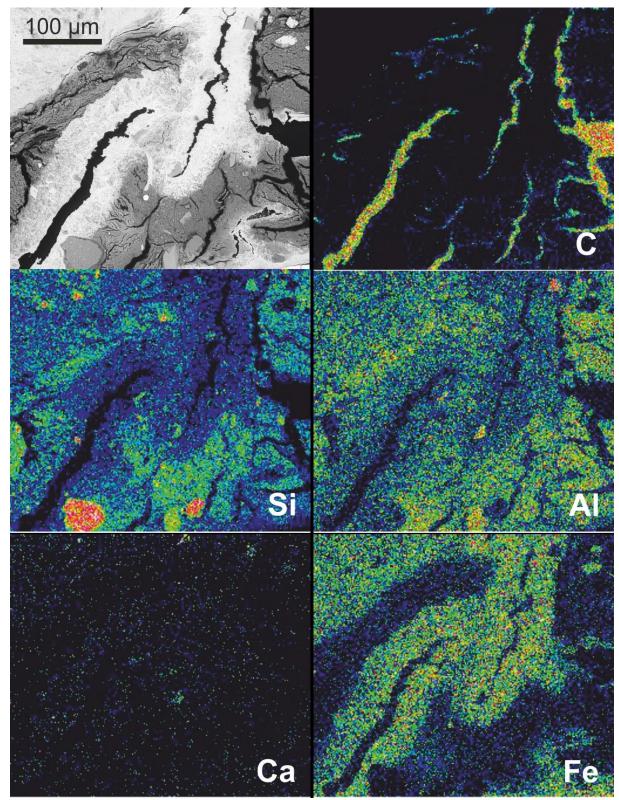


Figure 19 where the iron element map shows clear Fe-enhancment around microfractures. Around the steel filings themselves, Fe-enrichment was more colloform which is a typical texture of Fe corrosion and precipitation (Figure 18). There was evidence of Ca enrichment in some areas adjacent to the steel filings: this was quite pronounced in Figure 20, and was occurring adjacent to the steel/bentonite interface. No distinct crystalline calcium phase was observed.

Figure 21 illustrates the semi-quantitative EDXA microanalysis of the bulk bentonite along a profile approximately perpendicular to a bentonite-steel filing interface showing variations in concentration

(by weight) of iron, calcium and sulphur relative to aluminium. An average background value was also calculated from the average of three rastered fields of view of unaltered bentonite away from the far end of the bentonite plug, away from the filings, and plotted onto Figure 21 for comparison. The Fe/Al profile showed an enhancement in iron at the start of the profile where the steel filing has been corroded. This decreased rapidly within the first 20 μm into the bentonite where iron is close to detection limits. The S/Al displayed a similar distribution profile, with an enhancement of sulphur relative to aluminium within the first 7 μm , and then dropped rapidly to background levels. Neither the EDXA profile, nor the mapping, showed any evidence for the penetration of the sulphur into the bentonite, beyond ~ 20 μm . Calcium showed a slight enhancement in Figure 21 within the first ~40 μm from the interface with the steel filing, reaching a maximum at around 20 μm distance from the contact. No discrete Ca phase was observed within this region of slight calcium enhancement, and it appears that the Ca was hosted within the smectite clay mineral itself, which supports the evidence observed in the elemental mapping.

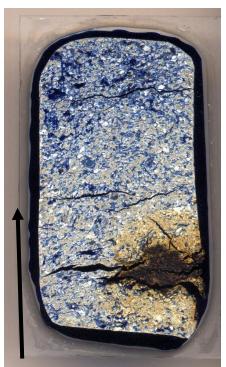


Figure 9. Scanned image of thin section clearly showing the extent of the brown/yellow staining on BUG021. Arrow shows flow direction. Note the staining is radial showing Fe-enrichment is by diffusion not advection. The sub-horizontal fractures are artefacts following dehydration during the sectioning process (these occur between layers in the bentonite due to preparation method). The sub-vertical fracture within the stained area only reaches to the edge of the staining and is roughly perpendicular to the other shrinkage fractures. This may be an enhanced original fracture/fluid pathway.

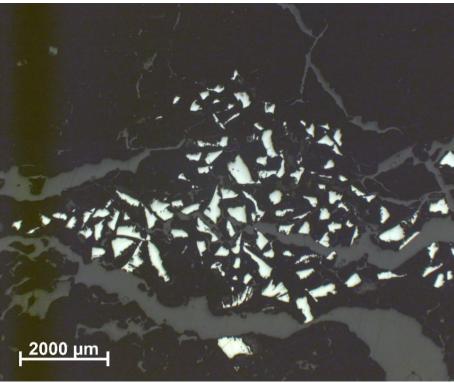


Figure 10. Optical photomicrograph (BUG021) in reflected light showing the positioning of the steel filings.

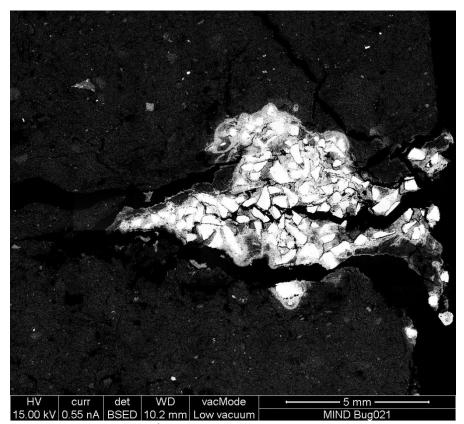


Figure 11. A BSEM montage of approximately the same area as Figure 10. The Fe enrichment and steel filings show as bright white. The Fe-enrichment appears far more limited than observed in the scan of the thin section. There is little or no detectable evidence of enrichment at this scale beyond a few 10s of microns around the steel filings under SEM imaging.

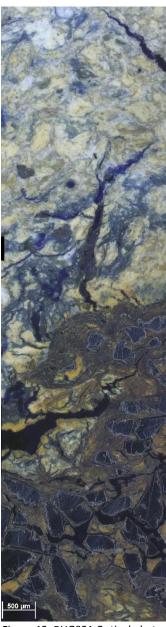


Figure 12. BUG021 Optical photomicrograph panorama in darkfield showing the transition from Fe-enriched bentonite around the steel filings, to unaltered bentonite at the top of the image. The steel filings appear very dark bluish grey in this image.

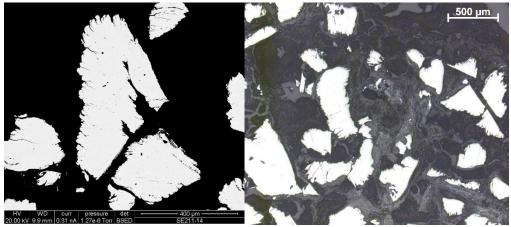


Figure 13 . Above: SEM image of the original steel filings starting material. Above right: optical image of BUG021 showing the enhanced embayed nature of the steel filings and reaction halos denoting the original boundaries of the steel filings.

Figure 14 Darkfield optical photomicrographs showing the effect of the Fe-enrichment on the bentonite in BUG021. A) The bentonite appears to be pelleted (probably a core of unhydrated bentonite), with enrichment lessening towards the cores of the pellets. B) Extensive corrosion of steel filings still has slivers of relict unaltered steel filings but the halo of altered steel filings shows the former extent of the particle.

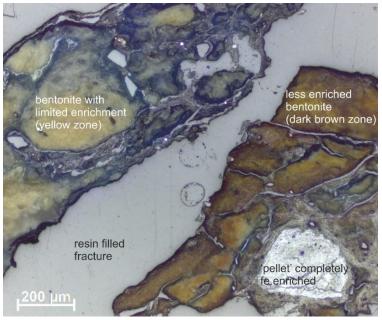


Figure 15 Darkfield optical photomicrograph showing a bentonite pellet in BUG021 which has been completely enriched in Fe (residual pellet), slightly less enriched bentonite which is within the dark brown zone surrounding the steel filings, and bentonite with limited enrichment within the yellow zone visible in the thin section scan.

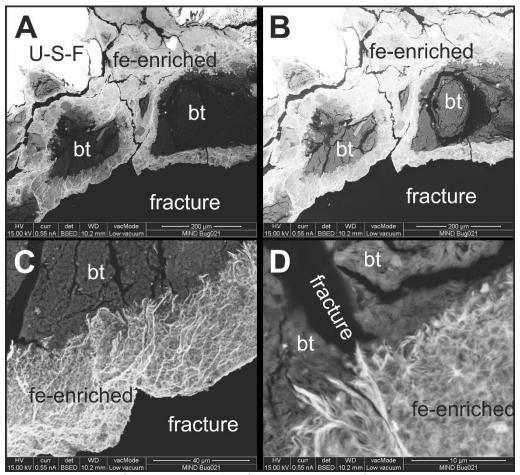


Figure 16. BSE images of BUG021 showing A) the fibrous Fe-enrichment of the bentonite which has penetrated from the edge of the 'pellets' inwards precipitating into shrinkage cracks up to ~40 µm wide. Shrinkage cracks occur due to the competition between bentonite wanting to hydrate and the Fe wanting to oxidise (the Fe tends to win – so bentonite dehydrates, and Fe precipitates into the shrinkage cracks around the edge). The relatively less hydrated bentonite (bt) cores show little Fe enrichment. B) a brighter image of A showing the texture of the bentonite cores. C) higher magnification of one of the rims from A showing the fibrous nature of the Fe enhancement, and D) high magnification showing the relatively abrupt boundary of the Fe-penetration which defines the dehydration front.

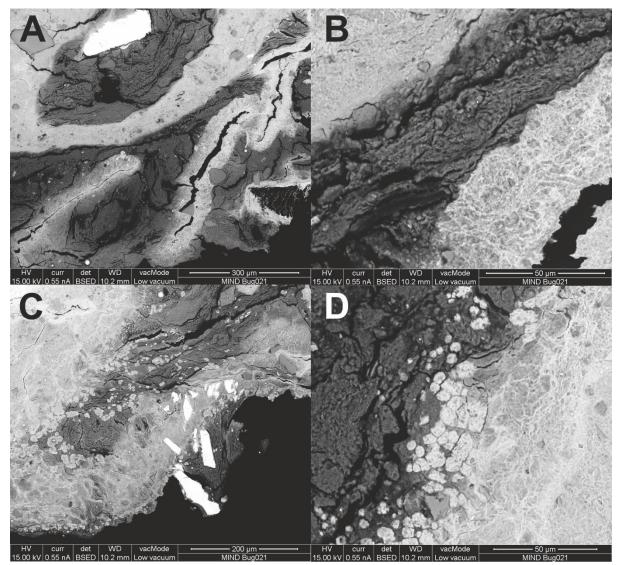
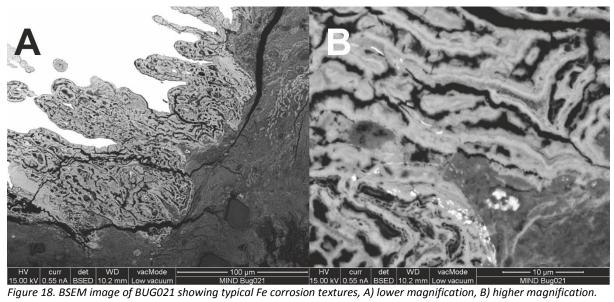


Figure 17. BSE image of BUG021 showing A) fractures which were original and acted as fluid pathways. Fe-enrichment is limited in extent either side of the fracture. At the top of the image is a rimmed bentonite pellet. B) high magnification view of the outer extent of a fracture showing the strong boundary to the Fe-enrichment. C) image showing the equant pelleted texture and D) a higher magnification view of this texture — pellets are probably due to nucleation of Fe oxyhydroxides followed by outward growth. Occurring along hydration front — may be due to a change in the hydration of the bentonite or density (some change in physical property) which means the Fe may not be able to diffuse so easily.



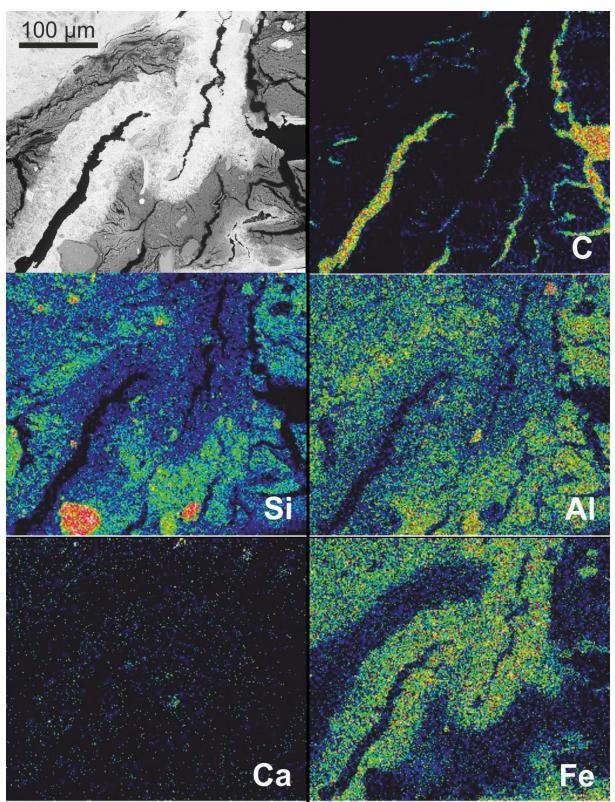


Figure 19 BSE high magnification image of microfractures within the bentonite of BUG021, and corresponding EDXA microchemical maps of the same area for carbon, silicon, aluminium, calcium and iron. The carbon map very clearly shows the resin infilled microfractures. The iron map clearly shows penetration of iron into the bentonite along the fractures, indicating that the fractures have acted as pathways for iron migration. Colour concentration scale: red = high concentration, blue / black = low concentration.

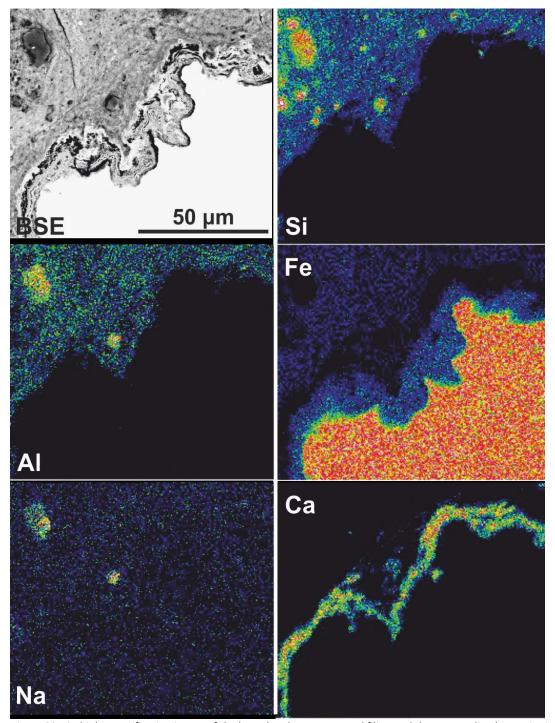
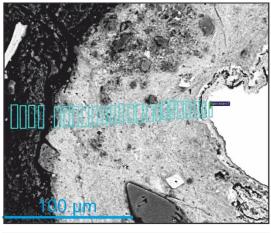
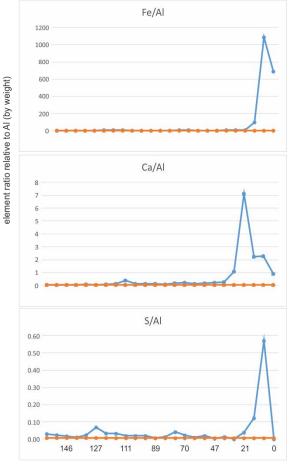


Figure 20 BSE high magnification image of the boundary between a steel filing and the surrounding bentonite in BUG021, and corresponding EDXA microchemical maps of the same area for silicon, aluminium, iron, sodium and calcium. The calcium map very clearly shows Ca precipitation which is probably calcium carbonate. Although clear crystal morphology is not visible, this may well be aragonite. Colour concentration scale: red = high concentration, blue / black = low concentration.





relative position of analysis in µm
Figure 21 BUG021 Montage of BSE image and plots of variation in element weight proportion ratios of Fe, Ca and S relative to Al (determined by EDXA) along a profile (blue line) through the bentonite taken perpendicular to the interface with a steel filing (right). The areas from which average rastered EDXA analyses were carried out are shown by the blue rectangles. The average background composition of the distal bentonite taken from three large area average rastered EDXA analyses from a distal, unaltered area is shown as an orange line.

3.2.2 BUG022 (1400 kg m⁻³ dry density, inoculated, no lactate)

This sample was sub-sampled for SEM characterisation by secondary electron imaging. Again, there was noticeable brown / yellow ferruginous staining around the iron filings (diffusive reaction). This was dark brown immediately surrounding the steel filings (steel filings) themselves (<1 mm

penetration into the bentonite beyond the steel filings), and this faded to a yellowish staining which penetrated the bentonite a further 5 mm beyond the steel filings (Figure 22 & Figure 23). The staining has penetrated in a radial nature around the steel filings – it is not one directional i.e. starting from the steel filings and penetrating in the direction of flow. This indicates Fe was moving by diffusion not advection. Optically this alteration did not appear so extensive – extending to around 2 mm. It takes very little Fe to produce staining, so this will be caused by fine dissemination of nanoparticles below optical and SEM resolution.

The secondary electron microscopy imaging of the stub sample revealed euhedral, acicular aragonite crystals growing from fracture walls into open pore space (Figure 24 & Figure 25). Although these fractures may have been enhanced by drying in the SEM vacuum, for these to grow, the fracture had to be present during the experiment. The Fe corrosion had consumed water, drying the bentonite and opening fractures adjacent to the steel filings. Carbonate has precipitated – with a morphology that suggests aragonite. The fluid contains some Ca, so this may have been derived from the pore fluids, or some may have come from exchangeable cation sites in montmorillonite

In addition to secondary acicular carbonate crystals growing into open pore space, this sample had a fibrous iron-rich phase within pore space around some grains, as well as a silica-rich (probably quartz) coating around some grains (see Figure 27 and Figure 28).

Figure 30 illustrates the semi-quantitative EDXA microanalysis of the bulk bentonite along a profile approximately perpendicular to a bentonite-steel filing interface showing variations in concentration (by weight) of iron, calcium and sulphur relative to aluminium. An average background value was also calculated from the average of three rastered fields of view of unaltered bentonite away from the far end of the bentonite plug, away from the filings, and plotted onto Figure 30 for comparison. The Fe/Al profile shows an enhancement in iron at the start of the profile where the steel filing has been corroded. This decreases rapidly within the first 7 μ m into the bentonite where iron is close to detection limits. The S/Al displays a similar distribution profile, with an initial enhancement of sulphur relative to aluminium which drops back rapidly to background levels. Neither the EDXA profile, nor the mapping (Figure 26 & Figure 29) showed any evidence for the penetration of the sulphur into the bentonite, beyond ~20 μ m. Calcium shows a slight enhancement in Figure 30 within the first ~30 μ m from the interface with the steel filing, reaching a maximum at around 7 μ m distance from the contact.

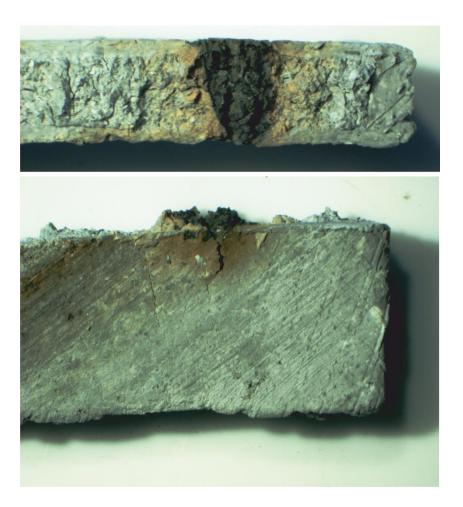


Figure 22. Photomicrograph of the sub sample of BUG022 used for secondary electron microscopy. There is a dark brown colouration of the bentonite surrounding the steel filings. Around this dark area is an area of lighter brown colouration which penetrates into the bentonite to \sim 2 mm.

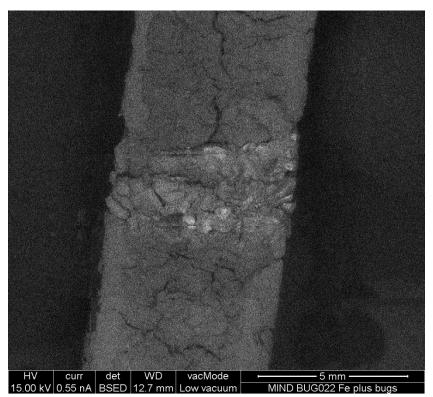


Figure 23. SEM montage of the stub in BSED showing the brighter Fe reaction area in the surrounding bentonite in BUG022.

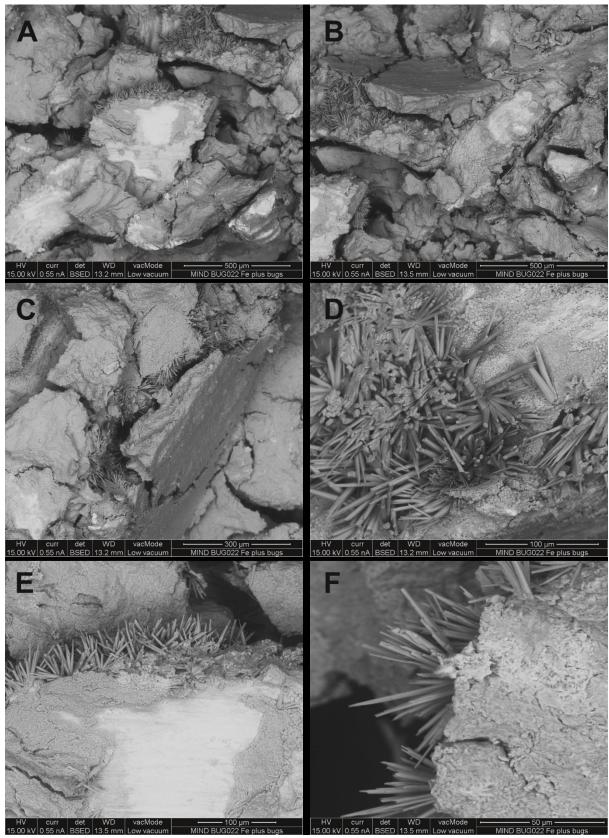


Figure 24. Secondary images of acicular aragonite precipitating into fractures developed during experiment BUG022. A-C show the aragonite coating fracture surfaces, D-F are higher magnification showing that the crystals have originated on the fracture walls and grown into the fracture space in a radial fashion. The crystals are up to 50 μ m in length.

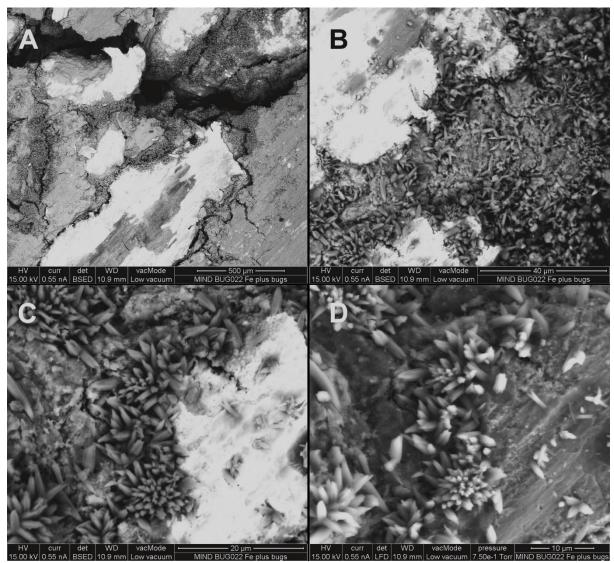


Figure 25. Detail of aragonite adjacent to steel filings showing the 'carpet' of crystals in BUG 022. A and B note the way the crystals have formed adjacent to the steel filings in and around the fractures. C-D detail showing the nature of the crystals and their growth into open pore space.

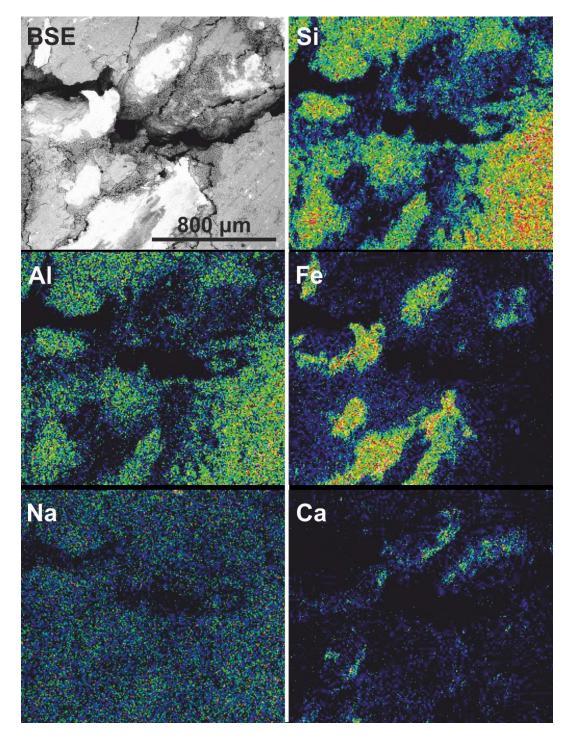


Figure 26. BSE high magnification image of the boundary between steel filings and the surrounding bentonite (BUG022), and corresponding EDXA microchemical maps of the same area for silicon, aluminium, iron, sodium and calcium. The calcium and iron maps very clearly show Ca (acicular aragonite) distribution in relationship to the Fe distribution. The Ca is adjacent to the Fe and has precipitated into open fractures / pore space. Colour concentration scale: red = high concentration, blue / black = low concentration.

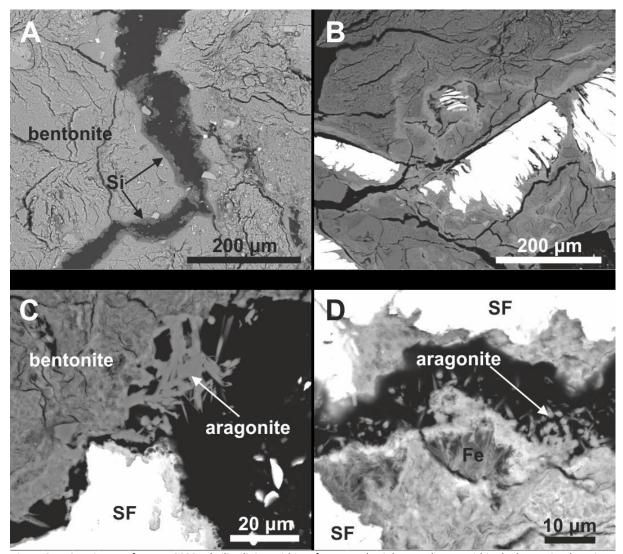


Figure 27. BSEM images from BUG022. A) silica lining within a fracture. B) Brighter pathways within the bentonite denoting Fe and Ca rich alteration of bentonite. C) aragonite adjacent to a steel filing and a fracture. D) Aragonite and fibrous Fe-rich material.

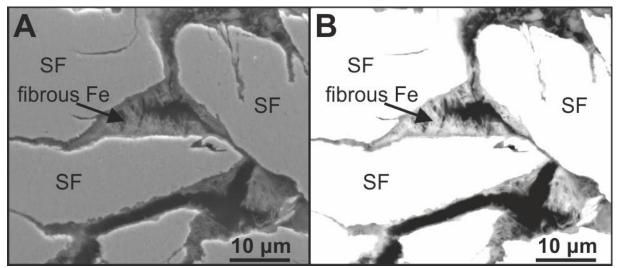


Figure 28. A) secondary image and B) BSEM image from BUG022 showing fibrous Fe coating around the steel filings.

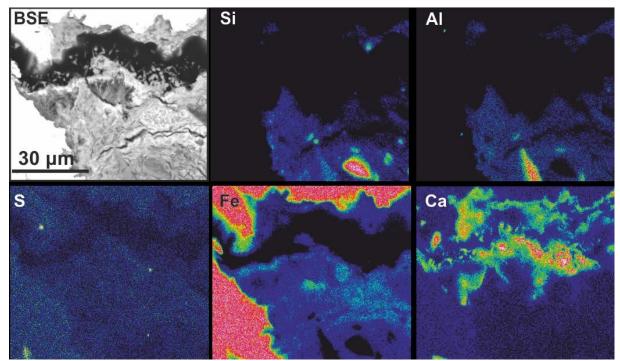


Figure 29. EDXA element map of the block from BUG022, showing Ca (aragonite) distribution in relationship to the Fe distribution. The Ca is adjacent to the Fe, and has precipitated into open fractures / pore space.

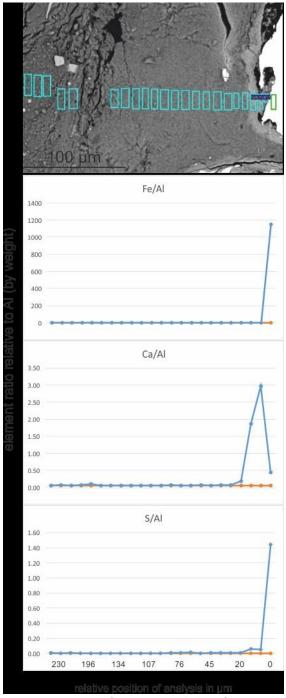


Figure 30. Montage of BSE image and plots of variation in element weight proportion ratios of Fe, Ca and S relative to Al (determined by EDXA) along a profile (blue line) through the bentonite taken perpendicular to the interface with a steel filing (right) in BUG022. The areas from which average rastered EDXA analyses were carried out are shown by the blue rectangles. The average background composition of the distal bentonite taken from three large area average rastered EDXA analyses from a distal, unaltered area is shown as an orange line.

3.2.3 BUG023 1400 kg m⁻³ lactate amended, sterile

This sample was sub-sampled for SEM characterisation by secondary electron imaging. There was very little noticeable brown / yellow ferruginous staining around the iron filings within the sub-sample immediately after removal from the experimental rig (Figure 31). It was noted that the brown staining became apparent following vacuum drying of the sample, indicating oxidation of the iron.

The stub sample showed noticeable brown staining, up to 20 mm away from the steel filings (Figure 32).

The secondary electron microscopy showed little in the way of alteration. The filings in this sample were extremely sparse, and only one or two were visible in the stub (Figure 33). Analysis on thin sections remains to be carried out in this sample.

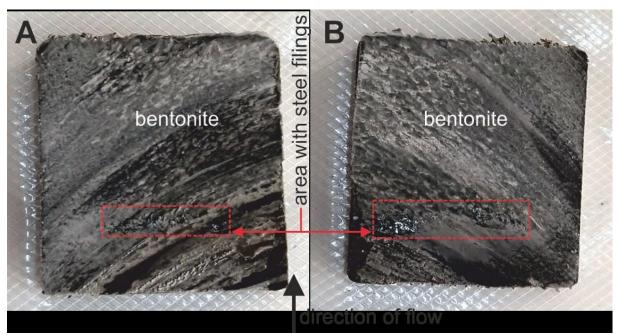


Figure 31. Photograph of both sides of the sub sample from BUG023 used for secondary electron microscopy. There is little discolouration of the bentonite surrounding the filings.

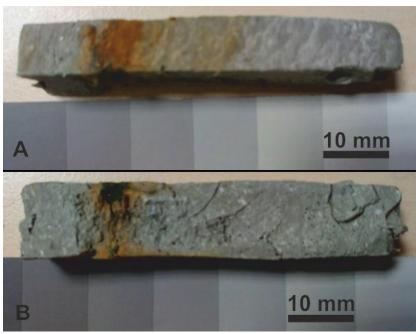


Figure 32. Photograph of the stub sample from BUG023 following drying. Fe-oxidation is apparent: brown discolouration is visible \sim 20 mm from the steel filings.

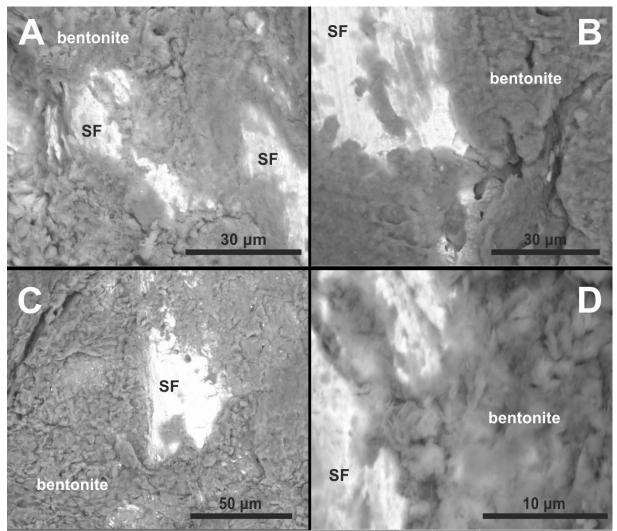


Figure 33. BSEM images from the stub sample from BUG023. Very little alteration observed. No visible Fe alteration and no aragonite.

3.2.4 BUG024 (1400 kg m⁻³ dry density, lactate amended, inoculated)

This sample was sub-sampled for SEM characterisation by secondary electron imaging. There was very little noticeable brown / yellow ferruginous staining around the iron filings within the subsample.

The secondary electron microscopy revealed euhedral, acicular aragonite crystals growing from fracture walls into open pore space (Figure 34). Although these fractures may have been enhanced by drying in the SEM vacuum, for these crystals to grow, the fractures had to be present and open during the experiment. It is known that Fe corrosion processes consume water, drying the bentonite and opening fractures adjacent to the metal.

Acicular calcium carbonate (probably aragonite) was also noted in the sample from BUG022, which was also inoculated. Aragonite has not yet been observed in the sterile samples, although calcium enrichment close to the steel filings has been observed in the elemental mapping.

In this sample, a wispy, fibrous Fe-rich material was observed in the stub samples (Figure 34B-D), that appears to have been precipitated over the layer of acicular aragonite. A fibrous Fe-phase was also noted in BUG022 precipitating around some grains, although it was not observed over the acicular layer. Analysis of thin sections from this experiment is yet to be carried out.

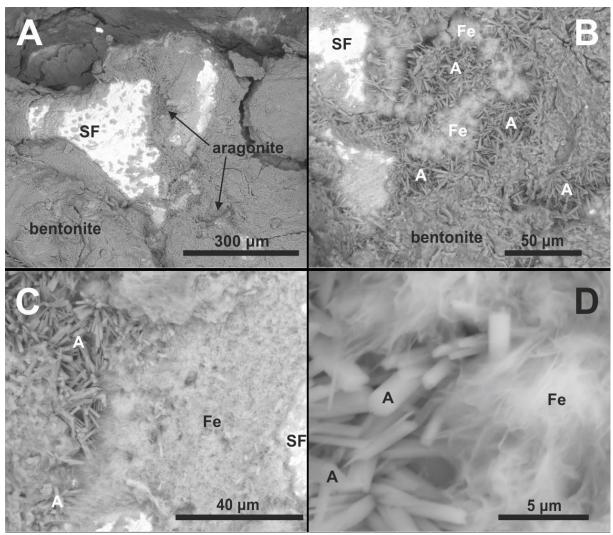


Figure 34. BSEM and secondary SEM images from stub from BUG024. A) SF = steel filing within the bentonite. Aragonite is present within fractures adjacent to the filing. B) SF=steel filing, A=aragonite, Fe= iron rich material. A fine, fibrous material is present which appears to have formed over the aragonite. EDXA indicates this is Fe rich. C) In places this Fe rich material is widespread and is completely covering the aragonite. D) High magnification view showing the acicular aragonite and the wispy, fibrous Fe-rich material.

3.3 XRD analysis

3.3.1 BUG021 uninoculated, no lactate added

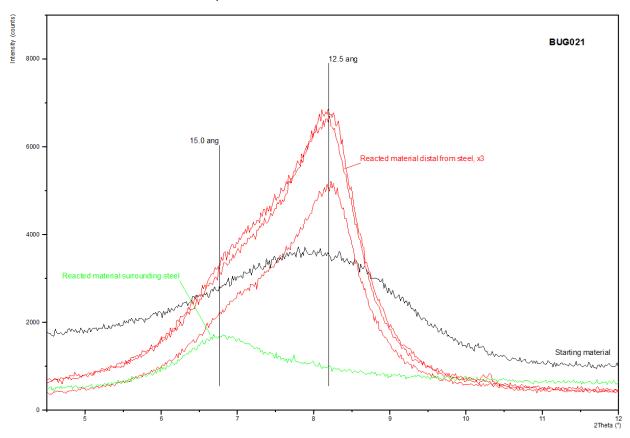


Figure 35. Zoomed view of low angle region of oriented mount XRD traces of starting material (black trace) and post experimental material from BUG021 (reacted material surrounding steel, green trace; reacted material distal from steel, red traces x3)

The starting material and subsamples taken distal to the steel alteration produced a $^{\sim}12.5$ Å smectite d₀₀₁ spacing, suggesting the presence of predominantly monovalent (Na, K) interlayer cations (Figure 35). Material taken from the bentonite – steel interaction zone produced a larger $^{\sim}15.0$ Å smectite d₀₀₁ spacing, suggesting the presence of predominantly divalent (Ca, Mg, Fe) interlayer cations.

3.3.2 BUG022 inoculated, 1400 kg m⁻³ no lactate added

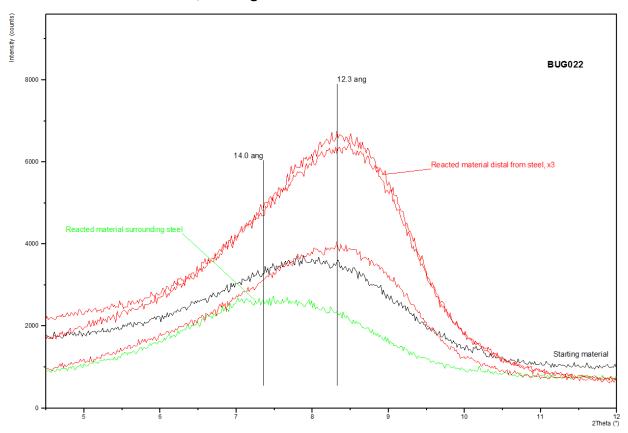


Figure 36. Zoomed view of low angle region of oriented mount XRD traces of starting material (black trace) and post experimental material from BUG022 (reacted material surrounding steel, green trace; reacted material distal from steel, red traces x3)

The starting material and subsamples taken distal to the steel alteration produced a $^{\sim}12.3$ Å smectite d₀₀₁ spacing, suggesting the presence of predominantly monovalent (Na, K) interlayer cations (Figure 36). Material taken from the bentonite – steel interaction zone produced a larger $^{\sim}14.0$ Å smectite d₀₀₁ spacing, suggesting the presence of predominantly divalent (Ca, Mg, Fe) interlayer cations.

3.3.3 BUG023 inoculated, 1400 kg m-3 lactate added

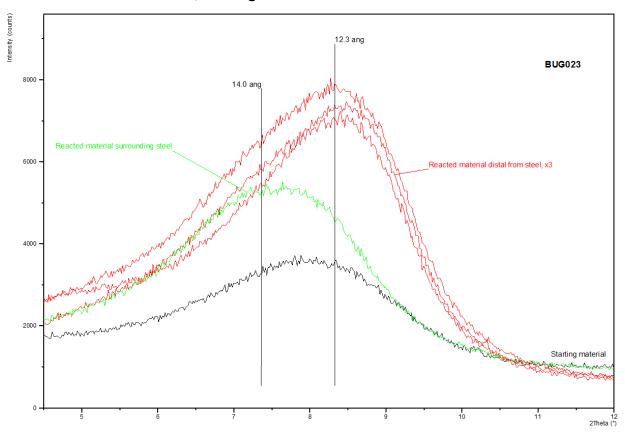


Figure 37. Zoomed view of low angle region of oriented mount XRD traces of starting material (black trace) and post experimental material from BUG023 (reacted material surrounding steel, green trace; reacted material distal from steel, red traces x3)

The starting material and subsamples taken distal to the steel alteration produced a \sim 12.3 Å smectite d₀₀₁ spacing, suggesting the presence of predominantly monovalent (Na, K) interlayer cations (Figure 37). Material taken from the bentonite – steel interaction zone produced a larger \sim 14.0 Å smectite d₀₀₁ spacing, suggesting the presence of predominantly divalent (Ca, Mg, Fe) interlayer cations.

3.4 Microbiological analysis

The results of the culture based enumeration of aerobic and anaerobic heterotrophs, sulphate reducing bacteria and iron reducing bacteria are shown below in Figure 38 and Figure 39. Following MPN counts for heterotrophs in the first pair of experiments (BUG021 and BUG022), difficulties were experienced distinguishing between cloudiness caused by the presence of clay and cloudiness as the diagnostic feature of heterotrophic growth. As both of these lead to a general trend of decreased cloudiness with increased sample dilution, there was the potential for confusing the two, therefore calling into question the reliability of these data. For BUG023 and BUG024 both MPN and Miles Misra methods were used. However, for those experiments it was impossible to distinguish between bacterial growth and clay causing the cloudiness in the MPN assays, so only the Miles Misra data are reported. Contrary to this general trend of over reporting numbers, there was no sign of cloudiness developing in the MPN for anaerobic heterotrophs in BUG021. The reasons for this is not clear, but is unlikely to reflect an absence of anaerobic heterotrophs given the detection of aerobic heterotrophs and iron reducing bacteria in some samples. Therefor this result should be treated with caution. Numbers of anaerobic heterotrophs were generally higher than aerobic heterotrophs in all experiments, as would be expected in an anoxic experiment. However there were significant numbers of aerobes detected, indicating a large proportion of facultative bacteria in these experiments. With the exception of BUG021 (discussed above) the number of anaerobic

heterotrophs was much higher in inoculated experiments than the "sterile" one. Anaerobic heterotrophs were detected in all sections of the inoculated BUG022 sample (952 – 305,914 cells ml⁻¹) and BUG024 (8312 – 29,750 cell ml⁻¹), but only in sample 1, 3 and 4 at lower densities (438 – 4,813 cells ml⁻¹) of BUG023. Similarly, aerobic heterotrophs were found throughout samples from inoculated experiments (BUG022 and BUG024) at higher cell densities (1,413-30,587 and 875-3,062 cells ml⁻¹ respectively) than the uninoculated BUG023 (417 – 833 cells ml⁻¹), where samples were only found in subsamples 4 and 5 of the clay sample. There was no evidence of the lactate amendment supporting greater numbers of heterotrophs.

For the two functional groups of bacteria (IRB and SRB), no bacteria were detected in the uninoculated BUG023 experiment and only IRB at low cell densities (767 – 919 cells ml⁻¹) in samples 1 and 2 of BUG021. The fluid in the injection pump (inflow fluid) and the back pressure pump (outflow fluid) remained sterile in all experiments except BUG022 where low numbers of SRB, anaerobic and aerobic heterotrophs were detected, and BUG021 where IRB were detected by the end of the experiment.

Anaerobic heterotrophs

Aerobic heterotrophs

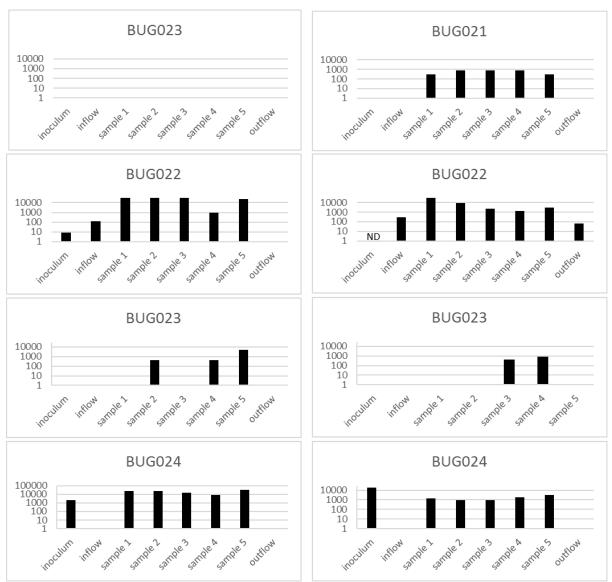


Figure 38 Enumeration of aerobic heterotrophs and an anaerobic heterotrophs in samples from experiments BUG021-BUG024. Refer to figure 5b for location of samples 1-5. N.B. BUG021 and BUG022 were counted by MPN, BUG023 and BUG024 were counted using a Miles Misra technique. The justification for this is outlined in 2.7.2. ND=not determined

Sulphate reducing bacteria

Iron reducing bacteria

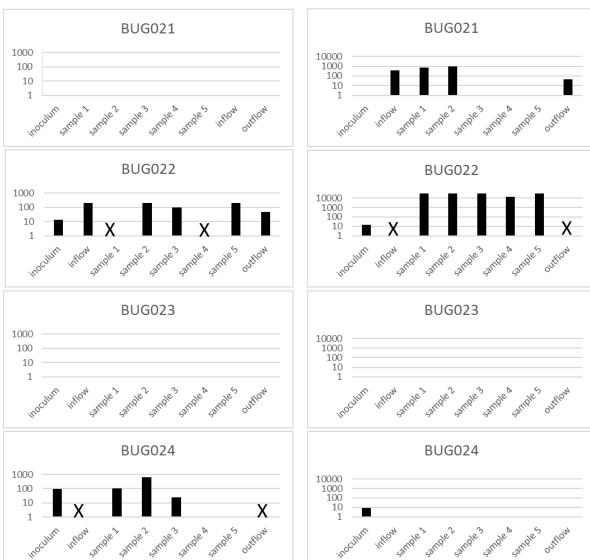


Figure 39 Enumeration of sulphate reducing bacteria and iron reducing bacteria in samples from experiments BUG021-BUG024. Refer to figure 5b for location of samples 1-5. X= invalid entry outside of range of MPN algorithm.

4 Discussion

SEM analysis showed alteration of the features around the corroded steel in all samples analysed so far. In hand specimens a clear stained zone appeared around the steel filings following drying of the sample. Hence it is likely that this staining is due to oxidation occurring during the preparation of samples/thin sections for SEM (e.g. compare Figure 31 with Figure 32). In the uninoculated experiment without lactate (BUG021), strong Fe enrichment was observed within the bentonite with Fe coating (or replacing) the bentonite. Some calcium precipitation was observed by element mapping, but no identifiable crystal morphologies observed. So far only stub analysis has been carried out on the uninoculated sample in the presence of sodium lactate (BUG023), but this did not reveal any obvious iron enrichment or calcium precipitation. In comparison to this, in both of the inoculated experiments, the material around the corroded steel was characterised by calcium enrichment (precipitation of acicular calcium carbonate crystals) within fractures in the bentonite next to the steel. In both cases crystals (probably aragonite) were observed in this fracture space. A fibrous iron-rich phase was observed in the bentonite, and in the case of the lactate amended, inoculated experiment, precipitating over the acicular calcium carbonate. The presence of crystals

growing into open space within fractures indicates that these fractures were open during the experiment. This is consistent with previous work (ref) which indicate that cracks open up around corroding steel as water within the bentonite is consumed by the corroding steel causing the clay to shrink back. This water movement may be responsible for the observed calcium enrichment and iron diffusion. In Milodowski et al. (2007) [28], the petrographical evidence indicated that Fe from the corroding steel displaced the Ca²⁺ from the exchangeable cation interlayer sites in the montmorillonite. The pattern of Ca distribution showed that the Ca concentrated in several bands around the steel wires. Initially, Ca was displaced from bentonite at the interface with the steel, or it migrated towards the corroding metal as Fe diffused into the bentonite. In addition, later bands of aragonite formed as more Ca²⁺ was displaced from the bentonite and was concentrated at the leading edges of the diffusive Fe fronts as Fe migrated away from the wire and into the bentonite matrix. These observations are consistent with potential mechanism for bentonite alteration under anoxic conditions, described previously by [29], [30], involving substitution of interlayer cations such as Na⁺ and Ca²⁺ by Fe²⁺ produced by iron corrosion. Studies that have looked at these corrosion processes from a purely abiotic perspective have observed the formation of aragonite either by XRF alone or also by the observation of distinctive crystal growth, yet no aragonite was observed in the two uninoculated (BUG021 & BUG023) experiments in this study.

It is interesting that in our experiments, only the samples inoculated with the SRB enrichment showed the growth of aragonite crystals. It is intended that further XRD analysis on the samples will provide addition information on the presence of aragonite in those samples where crystal growth was not observed (and confirm the identity of those where they were observed). On the basis of the results so far, the presence of aragonite cannot be conclusively linked to microbial activity in the inoculated samples (due to the limited number of experiments it has been possible to run). The absence of aragonite in the uninoculted experiments is curious as previous abiotic experiments already discussed observed aragonite without inoculation. There could be several explanations for this. Firstly, previous studies have not added microbes, but neither have the excluded them. In our experiments sterilisation by irradiation removed microbes from the system. Microbial enumeration at the end of the experiments suggested that this was not entirely successful, but nonetheless microbial numbers were much lower in the uninoculated samples. Secondly our experiments were much shorter than previous experiments, so it may simply be that there was not enough time for the aragonite to precipitate. Hopefully, evidence to support or refute this will be obtained from further experiments. Additionally, further XRD analysis and the results of microbial community analysis may provide evidence to suggest a mechanism of microbially induced aragonite precipitation.

It is not clear what effect the observed crystal growth could have on the swelling properties of the bentonite, but other changes observed from temperature and humidity-controlled, oriented mount XRD analysis of samples from the first three experiments (BUG021, BUG022 and BUG023) could indicate that the corrosion of steel within the clay could reduce the swelling capacity of the clay. The smectite in the zone with visible alteration, caused by the corrosion of the steel had larger basal spacings than both the starting material and the bentonite subsamples taken further away from this stained zone. This indicates that divalent cations have replaced monovalent cations in the bentonite around the steel, consistent with previous work e.g. [31] that has reported this replacement. Note that this occurred in all samples analysed so far, both inoculated and uninoculated and does not therefore appear to be under microbial control. This change in the valency of the interlayer cation could potentially affect the swelling capacity of the bentonite, affecting its function as a barrier material. However, in these experiments, the zone of alteration was rather small, and did not have any effect on the measured stress. In order to fully assess this, much longer experiments would be required to investigate if the zone of alteration increases over time, to the point at which it could alter the swelling capacity. Comparison of the two samples from experiments without lactate addition (BUG021 & BUG022) showed a slightly smaller d_{001} spacing in the inoculated experiment. This could indicate less divalent substitution when microorganisms are present, possibly related to the competition for calcium between interlayer substitution and the aragonite crystal formation

described above. However, it should be noted that with such a small difference in basal spacing, no firm conclusion should be drawn from this. Comparison of inoculated and inoculated samples that will be carried out in the remainder of this project may confirm the robustness of this observation. If this is a result of microbial activity, the mechanism through which this operated is not clear. The addition of sodium lactate to the groundwater also appeared to reduce the amount of divalent substitution. As with the inoculated/uninoculated experiments, this is a subtle change and interpretations are tentative at this stage, but this observation may relate to the increased amount of monovalent sodium ions present due to the addition of sodium lactate. Further XRD analysis will be carried out on these samples and may provide additional information about the non-clay minerals associated with the alteration zone and may confirm the presence of aragonite crystals observed by SEM.

General trends from the heterotroph counts show that low numbers of bacteria were found in the inflow and outflow samples. Both fluid started sterile, and flow was in the direction of injection pump to back pressure pump so some migration of microorganisms might have been expected into the backflow pump (outflow), the injection fluid should have remained sterile. However, heterotrophs were only detected in the inflow sample of BUG022 (inoculated, no lactate) sample and IRB in BUG022. Bacteria were also detected within the clay of the supposedly sterile clay samples. Although, precautions were taken to prevent contamination during set up, it was acknowledged that due to the complexity of the VCAF vessel, there remained a risk of microorganisms entering the system. Testing the irradiated clay indicated that no growth could be supported in anoxic or oxic conditions, so this is unlikely to be the source of contamination. It is possible that the contamination could arise from microorganisms persisting in gaps within the valves, joints or tubing between the injection pump and CVAF vessel. Generally the lack of microorganisms in the inflow and outflow fluids indicated that the method of sterilising the system by soaking in 70% methanol under a pressure of 1000 kPa is an effective sterilisation method, though clearly not perfect. Relatively low levels of aerobic and anaerobic organisms were found in the clay sample in the sterile experiments (BUG021 and BUG023). These were typically at least an order of magnitude lower than the corresponding inoculated experiment. This might indicate a potential route of entry of foreign bacteria during sample preparation. To ensure even consistence the clay was mixed with the groundwater in the anaerobic cabinet for 30 minutes. To protect the clay from contamination from organisms in the anaerobic cabinet atmosphere, sterile cling film was used to cover the clay during this process. It is possible that the samples became contaminated during this step. Although these samples did not remain completely sterile numbers were lower than the inoculated samples and microorganisms were not found throughout the core as they were in the inoculated samples, therefore the result give a valid comparison of low and high microbial numbers/activity. A similar pattern of lower cell numbers for SRB and IRB was observed in the sterile samples compared to the inoculated. For the BUG021 experiment (sterile, no lactate), no SRB were detected in any samples and for BUG023 (sterile, lactate amended) no SRB or IRB were detected, however, as no IRB were detected in the inoculated BUG024 experiment, despite detection of SRB (many of which have the genetic potential for iron reduction), there may have been some issues with the reliability of that assay. IRB were detected in BUG021 in both the inflow and outflow fluids and in samples 1 and 2, between the inlet to the sample and the steel, but numbers were relatively low. IRB and SRB were detected through the sample in BUG022, at numbers higher than the inoculated load. In BUG024 SRB numbers were similar or higher to the inoculum near the inlet and steel, but decrease towards the outlet, with no detection of SRB in sample 4 and 5. This indicates that, in at least part of the clay sample, microorganisms implicated in corrosion and clay alteration not only survive, but are also actively increasing their numbers. The observations obtained by culture based methods will be confirmed by qPCR analysis of 16s rRNA and functional genes at a later date. Whether this microbial activity plays a part in the observed aragonite precipitation and fibrous iron formation seen in inoculated experiments will be explored further in subsequent experiments.

Comparison of the evolution of swelling pressure through each test history, and the permeability values for each sample (Figure 7 & Table 4, summarised in Figure 40 Summary plot showing the change in swelling pressure (pre- and post-hydraulic testing) and the permeability values obtained for each test.) reveals a difference in the swelling pressure values for test BUG021. While it remains difficult to explain why these values are significantly lower than those for the rest of the test matrix, the data shows some interesting behaviour. By comparing the initial and post-test values we see that in BUG021 and BUG022 there is very little change. However, in BUG023 and BUG024 values for swelling pressure at the end of testing are significantly higher than those obtained prior to hydraulic testing, suggesting some form of reaction has occurred causing expansion of the fabric. It is possible that this could be related to the reduced amount of divalent substitution seen in the lactate amended samples (BUG023 & BUG024) and the higher proportion of remaining smectitic swelling clay. While SEM and XRD analysis suggest alteration of the mineral assemblages and the growth of aragonite, localised around the iron, the low compressibility or "stiffness" of the clay combined with the small amounts of mineral growth (and its associated expansion of the fabric) could result in a detectable increase in stress. Given the localised nature of corrosion within the clay, longer term testing of samples with iron dispersed within the sample are required to confirm and contextualise these results and its understand its potential impact on performance assessment.

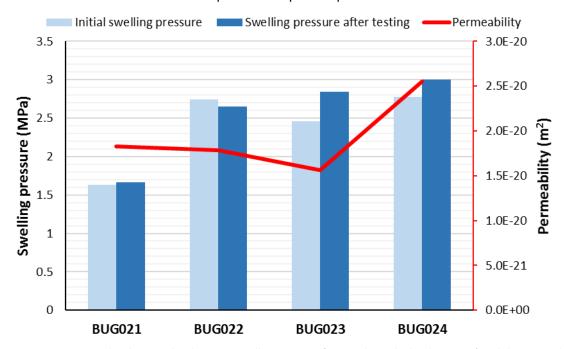


Figure 40 Summary plot showing the change in swelling pressure (pre- and post-hydraulic testing) and the permeability values obtained for each test.

The permeability data presented in Figure 5 suggests little in the way of any systematic change in behaviour from one test to the next. However, given the limited duration of the tests, this is not surprising as alteration of the bentonite was limited to a small zone adjacent to the iron. From a 'flow perspective' this will have little impact, as the bulk of the clay, and therefore the flowing porosity, remains unchanged. To understand the full impact of microbial action on the hydraulic properties of the clay, test durations would need to be increased substantially, or the iron should be dispersed within the entire clay matric to increase reaction rates. Given these findings, the question of whether microbial activity alters the hydraulic behaviour of bentonite remains unanswered. However, XRD and SEM analysis has identified alterations that appear to be related to the presence of microbial cells in the sample. This observations deserve further investigation, and will the focus of attention for the remainder of the project. However, further work is required beyond the lifetime of this project to fully assess the impact of microbially induced changes on the hydraulic integrity of the clay.

5 Acknowledgement

The MIND-project has received funding from the European Union's Euratom research and training program (Horizon2020) under grant agreement 661880 The MIND-project.

6 References

References

- [1] M. Libert, M. Kerber-Schütz, L. Esnault, and O. Bildstein, "Are Underground Clay Disposal Conditions Favorable for Microbial Activity and Biocorrosion?," *Procedia Earth Planet. Sci.*, vol. 7, pp. 73–76, Jan. 2013.
- [2] P. Humphreys, J. W. West, and R. Metcalfe, "Microbial effects on repository performance," 2010.
- [3] S. Stroes-Gascoyne and J. M. West, "Microbial studies in the Canadian nuclear fuel waste management program," *FEMS Microbiol. Rev.*, vol. 20, no. 3–4, pp. 573–590, 1997.
- [4] V. Boivin-Jahns and R. Ruimy, "Bacterial diversity in a deep-subsurface clay environment.," *Appl. Environ. Microbiol.*, vol. 62, no. 9, pp. 3405–3412, 1996.
- [5] I. Deniau, S. Derenne, C. Beaucaire, H. Pitsch, and C. Largeau, "Morphological and chemical features of a kerogen from the underground Mol laboratory (Boom Clay Formation, Oligocene, Belgium): structure, source organisms and formation pathways," *Org. Geochem.*, vol. 32, no. 11, pp. 1343–1356, Nov. 2001.
- [6] A. Bagnoud *et al.*, "Reconstructing a hydrogen-driven microbial metabolic network in Opalinus Clay rock.," *Nat. Commun.*, vol. 7, p. 12770, Oct. 2016.
- [7] L. Urios, F. Marsal, D. Pellegrini, and M. Magot, "Microbial diversity of the 180 million-year-old Toarcian argillite from Tournemire, France," *Appl. Geochemistry*, vol. 27, no. 7, pp. 1442–1450, Jul. 2012.
- [8] M. Lopez-Fernandez *et al.*, "Bacterial Diversity in Bentonites, Engineered Barrier for Deep Geological Disposal of Radioactive Wastes.," *Microb. Ecol.*, May 2015.
- [9] P. Masurat, S. Eriksson, and K. Pedersen, "Evidence of indigenous sulphate-reducing bacteria in commercial Wyoming bentonite MX-80," *Appl. Clay Sci.*, vol. 47, no. 1, pp. 51–57, 2010.
- [10] K. Wouters, H. Moors, P. Boven, and N. Leys, "Evidence and characteristics of a diverse and metabolically active microbial community in deep subsurface clay borehole water.," *FEMS Microbiol. Ecol.*, vol. 86, no. 3, pp. 458–473, Dec. 2013.
- [11] O. X. Leupin *et al.*, "Fifteen years of microbiological investigation in Opalinus Clay at the Mont Terri rock laboratory (Switzerland)," *Swiss J. Geosci.*, vol. 110, no. 1, pp. 343–354, Apr. 2017.
- [12] A. Bengtsson and K. Pedersen, "Microbial sulphide-producing activity in water saturated Wyoming MX-80, Asha and Calcigel bentonites at wet densities from 1500 to 2000kgm-3," *Appl. Clay Sci.*, vol. 137, pp. 203–212, 2017.
- [13] M. Motamedi, O. Karland, and K. Pedersen, "Survival of sulfate reducing bacteria at different water activities in compacted bentonite," *FEMS Microbiol. Lett.*, vol. 141, no. 1, pp. 83–87, Jul. 1996.
- [14] K. Pedersen, M. Motamedi, O. Karnland, and T. Sanden, "Mixing and sulphate-reducing activity of bacteria in swelling, compacted bentonite clay under high-level radioactive waste repository conditions," *J. Appl. Microbiol.*, vol. 89, no. 6, pp. 1038–1047, Dec. 2000.

- [15] S. Stroes-Gascoyne, C. J. Hamon, P. Maak, and S. Russell, "The effects of the physical properties of highly compacted smectitic clay (bentonite) on the culturability of indigenous microorganisms," *Appl. Clay Sci.*, vol. 47, no. 1–2, pp. 155–162, Jan. 2010.
- [16] J. E. Kostka, E. Haefele, R. Viehweger, and J. W. Stucki, "Respiration and Dissolution of Iron(III)-Containing Clay Minerals by Bacteria," *Environ. Sci. Technol.*, vol. 33, no. 18, pp. 3127–3133, Sep. 1999.
- [17] Z. Cui, K., Sun, S., Xiao, M., Liu, T., Xu, Q., Dong, H., ... & Zhang, "Cui, Kai, et al. "Microbial mineral illization of montmorillonite in low-permeability oil reservoirs for microbial enhanced oil recovery," *Appl. Environ. Microbiol.*, vol. AEM-00176., 2018.
- [18] J. N. Perdrial, L. N. Warr, N. Perdrial, M.-C. Lett, and F. Elsass, "Interaction between smectite and bacteria: Implications for bentonite as backfill material in the disposal of nuclear waste," *Chem. Geol.*, vol. 264, no. 1–4, pp. 281–294, Jun. 2009.
- [19] L. Esnault, M. Libert, O. Bildstein, C. Mustin, F. Marsal, and M. Jullien, "Impact of iron-reducing bacteria on the properties of argillites in the context of radioactive waste geological disposal," *Appl. Clay Sci.*, vol. 83–84, pp. 42–49, Oct. 2013.
- [20] C. Mulligan, R. Yong, and M. Fukue, "Some effects of microbial activity on the evolution of clay-based buffer properties in underground repositories," *Appl. Clay Sci.*, vol. 42, no. 3–4, pp. 331–335, Jan. 2009.
- [21] H. El Hajj, A. Abdelouas, B. Grambow, C. Martin, and M. Dion, "Microbial corrosion of P235GH steel under geological conditions," *Phys. Chem. Earth, Parts A/B/C*, vol. 35, no. 6–8, pp. 248–253, Jan. 2010.
- [22] P. Rajala, M. Bomberg, M. Vepsäläinen, and L. Carpén, "Microbial fouling and corrosion of carbon steel in deep anoxic alkaline groundwater," *Biofouling*, pp. 1–15, Feb. 2017.
- [23] P. Rajala, L. Carpén, M. Vepsäläinen, M. Raulio, E. Sohlberg, and M. Bomberg, "Microbially induced corrosion of carbon steel in deep groundwater environment," *Front. Microbiol.*, vol. 6, Jul. 2015.
- [24] D. Féron and D. Crusset, "Microbial induced corrosion in French concept of nuclear waste underground disposal," *Corros. Eng. Sci. Technol.*, vol. 49, no. 6, pp. 540–547, 2014.
- [25] J. Miles, AA; Misra, SS; Irwin, "The estimation of the bactericidal power of the blood," *J. Hyg. (Lond).*, vol. 38, no. 6, pp. 732–749, 1938.
- [26] F. T. Madsen, "Clay mineralogical investigations related to nuclear waste disposal," *Clay Mineral.*, vol. 33, pp. 109–129, 1998.
- [27] L. E. Goldstein J I, Newbury D E, Echlin P, Joy D C, Fiori C, Scanning Electron Microscopy and X-Ray Microanalysis. Plenum Press, New York. 1981.
- [28] A. E. Milodowski *et al.*, "Mineralogical investigations of the interaction between iron corrosion products and bentonite from the NF-PRO Experiments (Phase 1) (2009) Svensk Kärnbränslehantering AB Technical Report TR-09-02."
- [29] S. T. Kamei G, Oda C, Mitsui S, Shibata M, "Fe(II)-Na ion exchange at interlayers of smectite: adsorption-desorption experiments and a natural analogue," *Eng. Geol.*, vol. 54, pp. 15–20, 1999.
- [30] A. T. Idemitsu K, Yano S, Xia X, Kikuchi Y, Inagaki Y, "Migration behaviour of iron in compacted bentonite under reducing condition using electromigration," *Mater. Res. Soc. Symp. Proc.*, vol. 757, p. II3.7.1–II3.7.8, 2003.
- [31] Smart, N. R. et al., "The anaerobic corrosion of carbon steel in compacted bentonite exposed